A

Dissertation on

Optical and photocatalytic properties of undoped and Ca doped $NaNbO_3$

Submitted in the partial fulfilment of the requirements for award

of degree of

Master of Science

in

Physics

(2016-2018)

Submitted by

Neha Rani

(301604030)

Under the guidance of

Dr. O. P. Pandey

(Senior Professor)

SCHOOL OF PHYSICS AND MATERIALS SCIENCE

THAPAR INSTITUTE OF ENGINEERING AND TECHONOLOGY

PATIALA (PUNJAB)-147004

July, 2018

CERTIFICATE

This is to certify that this dissertation entitled **"Optical and photocatalytic properties of undoped and Ca doped $NaNbO_3$"** which is being submitted by **Ms. Neha Rani (301604030)** in fulfilment of the requirements for the award of the degree of Master of Science M.Sc. in Physics from School of Physics and Materials Science, Thapar Institute of Engineering and Technology, Patiala, (Punjab), India. It is an exclusive record of candidate's own research work under the supervision of **Dr. O. P. Pandey.** The dissertation in part or in full has not been submitted in any other university or institute for the award of any degree.

Dr. O. P. Pandey

(Supervisor)

Senior Professor

School of Physics and Materials Science

Thapar institute of engineering and technology, Patiala

DECLARATION

I hereby declare that the work been presented in this thesis report entitled **"Optical and photocatalytic properties of undoped and Ca doped $NaNbO_3$"** by me in partial fulfilment of the requirements for the award of degree of **Masters of Science** in **Physics,** Thapar Institute of Engineering and Technology, Patiala is an authentic award record on my work carried out under the supervision of **Dr. O. P. Pandey**, Senior Professor, School of Physics and Materials Science, Thapar Institute of Engineering and Technology, Patiala. The matter presented in this report has not been submitted in any other university/institute for award of Master of Science or any other degree.

Neha Rani

Neha Rani

Regd no: 301604030

ACKNOWLEDGEMENT

After an extensive period of six months, I take this opportunity to write this note as a final touch of dissertation to express my gratitude and acknowledge the individuals who have been there for me in the completion of my thesis. These past few months were intense for me not only in the scientific but also on a personal level. The realm of time has taught me a lot and this dissertation has had a big impact on me. I would like to commence by thanking the people who helped me throughout this period. Prima face, I would like to thank my mentor and guide **Dr. O. P. Pandey** (Senior Professor, School of Physics and Materials Science) for his valuable guidance and constant support throughout the course of this work.

It is my privilege to thank **Prof. Prakash Gopalan**, Director, Thapar Institute of Engineering and Technology, Patiala, for providing the resources for my research work. I would also like to thank **Dr. Manoj Sharma** for their valuable support and help throughout the dissertation. I would also like to thank **Mr. Aayush Gupta** for embarking on this journey with me and staying with me till the end, no matter how I felt, he was there for me throughout. My lab mates at functional materials lab, were my constant source of encouragement and so I would also like to thank **Mr. Rameez Mir, Mr. Piyush Sharma, Ms. Ruby Priya, Ms. Navpreet Kaur, Ms. Jaspreet kaur** for thesis co-operation and help. Thank you for being there in all the ups and downs.

The greatest thanks go to my family members for their infinite support at each and every part of my life. Above all I express my indebtness to the almighty for all his blessings.

Neha Rani

Neha Rani

ABSTRACT

The adverse effect of growing industrialization has resulted in many environmental, economical and social problems such as global warming etc. To protect the environment and also to resolve these issues, it is necessary to find some good and highly efficient techniques for the treatment of waste water and harmful substances. In order to address these, some catalytic processes have been developed. Among all the known materials, peroveskite ABO_3 type of structures viz. $NaNbO_3$ holds special importance because of its nontoxic nature and high photocatalytic properties which can be used for dye degradation, CO_2 conversion and hydrogen generation. It also exhibits ferroelectric and piezoelectric properties. In the present study, undoped and Ca-doped (0.5%-2.0%,4.0%,6.0%) sodium niobate nanoparticles have been synthesized through chemical precipitation method using ammonium niobate oxalate hydrate ($C_4H_4NNbO_9.xH_2O$) and sodium sulphide (Na_2S) as niobium and sodium source, respectively. Various experiments were performed by varying the molar ratio (1:1,1:2,1:5,1:10,1:15,1:20,1:25) at different temperatures (600,700 and 800˚C) for the holding time of 5h. The phase composition, band gap and morphology are investigated by using X-ray diffraction (XRD), UV-visible spectroscopy, field emission scanning electron microscopy (FESEM) and transmission electron microscopy (TEM) respectively. XRD and electron microscopy confirmed the formation of faceted orthorhombic $NaNbO_3$ at 800˚C with the average crystallite size of 23.43 nm. UV–visible absorption spectroscopy showed the optical band gap 3.44 eV and 3.24 for undoped and Ca doped $NaNbO_3$, respectively. Synthesized nanoparticles were used as a photocatalyst to study the photocatalytic degradation of methylene blue dye under visible radiation. Firstly, the concentration of photocatalyst (undoped $NaNbO_3$) has been optimized to degrade 400 mg/L in solution of MB dye (1 mg/L). Now, the degradation of MB dye has been studied with undoped, Ca doped $NaNbO_3$ nanoparticles. From the results, it has been found that Ca doping concentration of 1.0% is optimal for its higher photo physical and photocatalytic properties. Catalyst shows the maximum photo degradation of MB dye in 6h under visible radiation.

List of Figures Page

List of Tables page

Chapter 1

Chapter 3

Chapter 4

Table of contents

Chapter 3

28-34

Chapter 4

35-60

Chapter 5

Chapter 6

1. Need for waste water treatment:

The global rise in industrialization in the past few decades has brought many social and economic problems which in turn has affected the environment. Water pollution occurs via contamination of water, industrial discharge of harmful chemicals and removal of toxic organic pollutants such as dyes, phenols, ethers etc. [1]. Residual dyes which are being generated from paper and pulp, textile, bleaching industries etc. are being directly exposed to natural water resources. Moreover, these sources of contamination are quite stable and non-self-degradable in natural conditions. So to remove such sources of contamination, many processes have been suggested such as flocculation, ultra filtration, reverse osmosis etc [2]. Demand of safe water for the healthy ecosystem, household and industrial utilization purpose is increasing as the population and industrialization have been increasing with time. To protect the environment and to resolve these issues, first technique i.e. conventional waste water treatment was developed. But this treatment did not work properly for the removal of toxic organic pollutants and harmful chemicals. So, it was necessary to find some better and highly efficient alternate techniques for the treatment of waste water and harmful substances. Many different techniques were investigated for such disastrous issues of mankind. Among them waste water treatment by photo degradation process has proven to be highly efficient because of its easy approach, low cost, better efficiency along with reusability of catalyst [3, 4].

1.1 Catalysis

Catalysis can be referred as a chemical reaction which can be accelerated/de-accelerated with the help of some external reagent which does not participate in the reaction, termed as catalyst [5]. The main purpose of the use of catalyst during any chemical reaction is to provide its external surface as platform to enhance the productivity of that particular chemical reaction. Further, based on the nature and phase present in the catalyst it can be categorized into two different categories which have been discussed as follows:

1.1.1 Types of catalysis:

Catalysis can be categorized into two types based on the performance of the catalyst i.e. positive catalyst and negative catalyst. Positive catalysis can be defined as catalysis in which the rate of chemical reaction increases by the addition of catalyst while, Negative catalysis is the one in which the rate of chemical reaction decreases upon the addition the catalyst. Another category of catalysis includes an auto catalyst in which any component itself acts as a catalyst when forms as a product

in a chemical reaction [6]. Moreover, it is environmentally clean and can be easily controlled based on the physical state of the catalyst. Catalysis process can be further divided into two categories depending upon the physical state of catalyst which are explained below:

1.1.1(a) Homogeneous catalysis: The reaction, in which the reactant and the catalyst are in the same phase, catalyst is referred as homogeneous catalyst and such catalysis is known as homogeneous catalysis. For example;

$$N_2 \uparrow + 3H_2 \uparrow \xrightarrow{CO\uparrow} 2NH_3 \uparrow \quad (1.1)$$

In the above reaction, the reactants nitrogen (N_2) and hydrogen (H_2) both are in gaseous phase and the catalyst i.e. carbon monoxide (CO) is also in gaseous phase resulting homogeneous catalytic production of NH_3 [5].

1.1.1(b) Heterogeneous catalysis: The reaction in which the reactant and catalyst are in different phases, is known as heterogeneous catalysis. These phases not only include solid, liquid and gases but, also used for immiscible liquids such as oil and water.

For example: Haber's process for the synthesis of NH_3.

$$N_2 \uparrow + 3H_2 \uparrow \xrightarrow{Fe(solid)} 2NH_3 \uparrow \quad (1.2)$$

In this reaction, the reactants N_2 and H_2 both are having gaseous phase while iron (Fe) which is acting as a catalyst has solid phase. So, these types of reactions fall under the category of heterogeneous catalysis.

Typical heterogeneous catalysts are the inorganic solids (i.e. metal salts, oxides, metals, sulphide etc.). This may also include organic materials i.e. ion exchanger, enzymes and organic hydroxides etc. As compared to the homogeneous catalyst, extraction and reuse of heterogeneous catalysts is more feasible, but its characterization and optimization is quite a tedious task.

1.2 Effect of catalyst on the reaction rate: It is well known fact that certain amount of energy is required for the initiation of chemical reaction, is known as activation energy (E_a). It is defined as the energy difference between the reactant and transition state (uncatalyzed reaction). Activation energy provides a medium for reactants in forming products (unless reactants themselves are reactive at ambient conditions) as shown in **Figure 1.1**. The difference in energy between the reactants and products represents as the ΔH. But ΔH does not depend on the rate of the chemical reaction. The reaction becomes exothermic when the activation energy of product become lower than that of reactant. In the overall reaction, the energy is released. The reaction becomes

endothermic when the activation energy of product become higher than that of reactant, so in the overall reaction the energy is absorbed. The addition of catalyst in the chemical reaction provides an additional platform (new shortcut path) for the reactants to form products which have lesser activation energy as compared to the un-catalyzed reaction and that reaction is known as catalyzed reaction. The activation energy of catalyzed reaction becomes less and takes less time for the completion of the reaction [7].

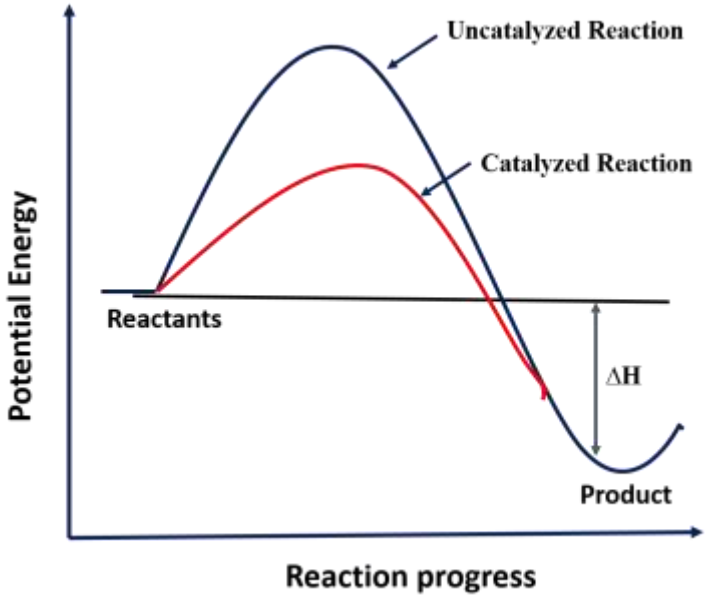

Figure 1.1: General representation of Gibb's free energy during a chemical reaction.

1.3 Characteristics of catalyzed reaction: Some of the specific features which are observed in a catalytic reaction are mentioned as follows;

(i) A small amount of catalyst is needed for the reaction to proceed.
(ii) Catalyst is not consumed in the reaction.
(iii) Catalyst does not start the reaction.
(iv) Catalyst does not alter the equilibrium conditions of the chemical reaction.

1.4 Photocatalysis

Photocatalysis is an efficient technique for waste water treatment than other conventional processes because it has ability to oxidize the organic pollutants into the harmless or nontoxic products [8]. Photocatalysis can be defined as the chemical reaction which is catalyzed in the

presence of photons. Photocatalyst should be non-toxic nature, highly stable and corrosion resistant. Moreover, it should exhibit ability to treat high concentrations of waste water [9]. In 1980, Salmon subdivided the photocatalysis into two categories, it includes photo generated catalysis and catalyzed photolysis.

For waste water treatment, new technology has been developed that is known as advanced oxidation process (AOP). It has also attracted much attention because of its ability to convert the pollutants into the non-toxic products directly from the waste water. AOPs are operated through the formation of radicals like hydroxyl radical, superoxide anion radical, electrons, holes etc. Hydroxyl radical is a very strong oxidizing radical [10]. It can destroy the pollutants and even those organic contaminants which are present in the water. Among all AOP processes heterogeneous photocatalysis has high efficiency in degrading wide range of organic contaminants into carbon dioxide, water and mineral acids. The use of heterogeneous photocatalysis has increased rapidly, with the various developments especially in relation to the environment and the energy. In 1972, Fujishimna and Honda [11] discovered the water splitting by using TiO_2 electrode under ultraviolet radiation into H_2 and O_2. Photo catalysis is the more convenient technique than conventional redox reactions due to following reasons:

- In a conventional redox reaction, both oxidizing agent and reducing agent react separately, but in photocatalysis both oxidation and reduction reactions occurs simultaneously.
- The conventional reaction is a multi-step reaction, but the photocatalysis is a single step reaction.
- In a conventional reaction many solvents are used but in photochemical reaction, we generally use water as solvent because other solvents are expensive.
- For photocatalyst activation, we use UV -visible radiation or visible radiation so that they can generate strong oxidizing agents in aqueous medium.

1.5 Semiconductor based photocatalysis

In semiconductors, the valence band is completely filled with electrons whereas the conduction band is completely empty. The energy difference between the top of the valence band and bottom of the conduction band is known as band gap energy. The relation between the band gap and the light absorption of the semiconductor is $\lambda=1244/E_g$ (in eV). For example, the band gap of $NaNbO_3$

is 3.4 eV and the corresponding wavelength is 364.70nm (UV region) as the range of UV region is in between 200-400nm [9].

When the energy of the incoming photons is equal to or greater than the band gap energy of the semiconductor, electrons are excited from the filled valence band to the empty conduction band. For different semiconductor materials, different energies are required for the excitation of the electrons from the valence band to the conduction band. After the excitation of electrons, conduction band is partially filled and the electrons can move freely in the conduction band. There is a positive hole left behind in the valence band and negative electron in the conduction band. In photocatalysis, it is known that there is a simultaneous oxidation and reduction processes. The hole lying in the valance band reacts with the surface bound H_2O and OH^- ions. They produce powerful oxidizing agents such as hydroxyl radical [4]. On the other hand, the electron in the conduction band reacts with the oxygen species, produces superoxide anion radical which is highly reactive. The whole process has been explained in **Figure 1.2**.

Electron hole pair generation

$$\text{hv} + \text{photocatalyst} \rightarrow e^- + h^+ + \text{photocatalyst}$$

Recombination of charge carrier

$$e^- + h^+ \rightarrow \text{Heat} + \text{Radiation}$$

Superoxide free anion radical

$$O_2 + e^- \rightarrow .O_2^-$$

Hydroxide free anon radical

$$h^+ + H_2O \rightarrow H^+ + HO.$$

$$h^+ + OH^- \rightarrow .OH[12]$$

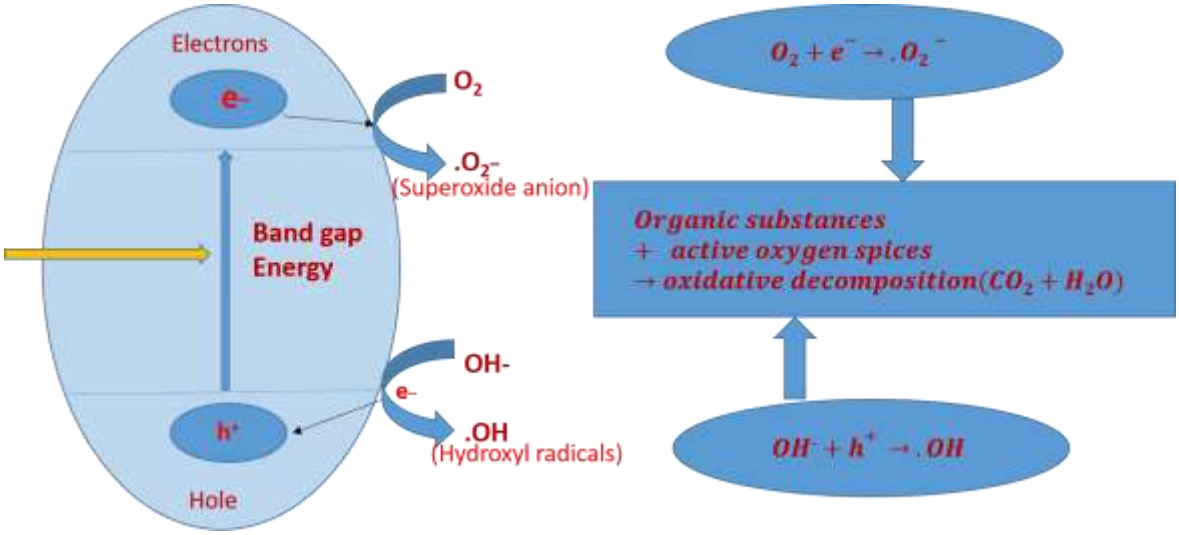

Figure 1.2: Mechanism of photocatalysis [13].

Metals, semiconductors and insulators can act as photocatalysts based on the requirement of the photochemical reaction. The band gap of the semiconductors lies in between the metals and insulators. Moreover, semiconductors are being used more than others. Because electrons can easily be excited from the valence band to the conduction band so, semiconductor materials act as a best medium to generate $e^{-}h^{+}$ pair upon irradiation than that of metals and insulators as shown in **Figure 1.3**. The band gap of semiconductor lies in between 2-4 eV. Various semiconductors like Oxides (ZnO, SiO_2, ZrO_2, TiO_2, Nb_2O_5, CeO_2 and NaNbO3 etc.), Sulfides (CuS, ZnS, CdS) and CdSe are used as photocatalyst. Moreover, some of the major semiconductors which are being used as photo catalyst are listed in **Table 1.1.**

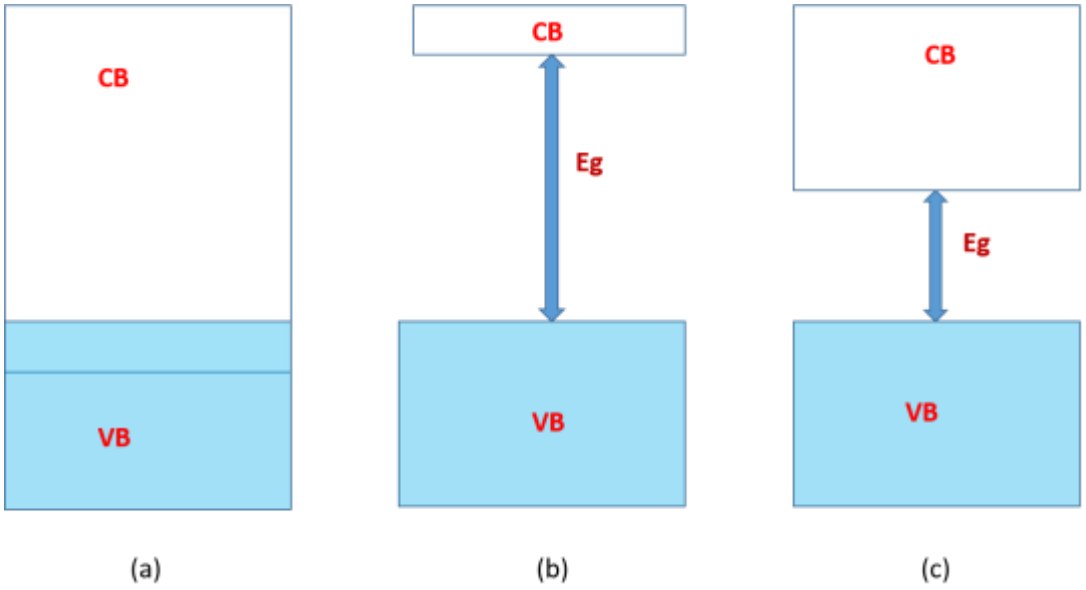

Figure 1.3: Band diagram of (a) metal (b) insulator and (c) semiconductor [14].

Table 1.1: Band gap energies of semiconductor material [15].

Photocatalyst	**Band gap (eV)**	**Photocatalyst**	**Band gap(eV)**
TiO_2	3.02	WO_3	2.76
ZnO	3.20	ZrO_2	3.87
CdS	2.58	SiC	3.00
ZnS	3.70	V_2O_5	2.70
Nb_2O_5	3.7	SnO_2	3.50
$NaNbO_3$	3.4	$SrTiO_3$	3.40
CdSe	1.70	Fe_2O_3	3.10

1.6 Photocatalysis versus photosynthesis:

The most familiar and common photocatalytic process is the photosynthesis process (production of O_2 in the presence of sunlight by plants). In this process chlorophyll, which is present in green leaf, act as a natural photocatalyst. In natural photocatalysis, chlorophyll absorbs sunlight and converts water (H_2O) and carbon dioxide (CO_2) into oxygen (O_2) and glucose ($C_6H_{12}O_6$). But in artificial photocatalysis, photocatalyst absorbs electro-magnetic radiations (i.e. UV or visible) to

generate electrons or holes to provide several oxidizing agents to decompose different organic compounds (phenols, esters, dyes etc.) and turn into CO_2 and H_2O [16]. A schematic representation of both mentioned photocatalytic processes has been shown in **Figure 1.4**.

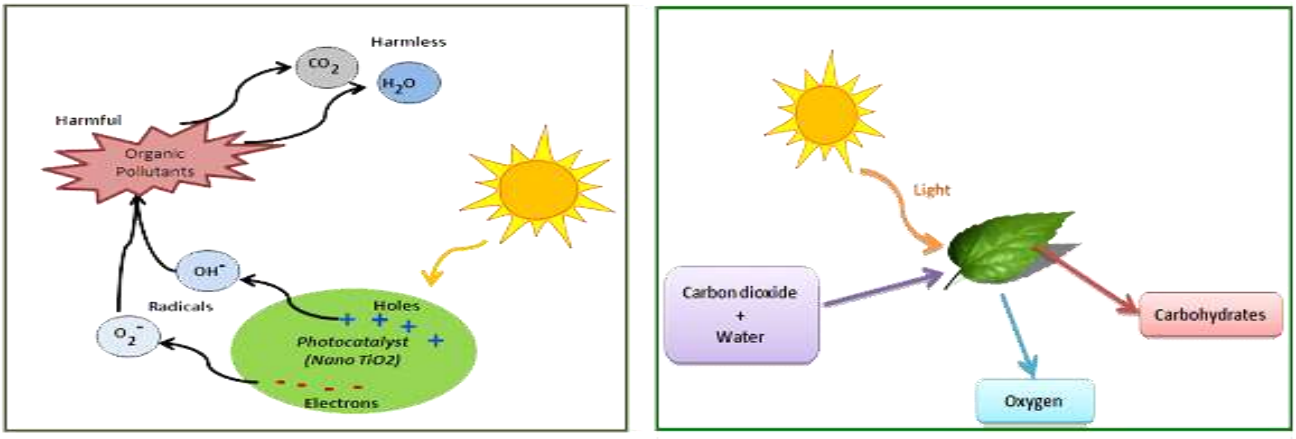

Figure 1.4: Comparison of photocatalysis and photosynthesis [17].

1.7 Applications of photocatalysis

Photocatalyst is being used in various engineering applications from automotive industries to medicinal purposes. Some of them are being discussed as follows:

1.7.1 Defogging glass: This problem can be easily visualized during the rainy season in side view mirrors of vehicles. During the rainy season these water droplets get strike to the mirrors and make the mirror blur but in the night these water droplets reflect the beam of headlights. During the day time, when the small amount of UV light falls on the surface of TiO_2, (fine coating on the mirror) the mirror surface becomes hydrophilic. But this process works only in day time, after sunset or dark places they create much difficulty. To recover this problem for night, silica is added to the surface of TiO_2 as the SiO_2 has the tendency to absorb the water molecules [18].

1.7.2 Air purification: For the elimination or reducing the polluted compounds in air, TiO_2 for the treatment of NO_x, SO_x, cigarette smoke etc is used as photocatalyst. To keep the walls of buildings, tunnels and lamp houses, a coating of TiO_2 is done. In the presence of sunlight atmospheric constituents such as NO_x, SO_x undergo the photochemical degradation and keep the walls clean.

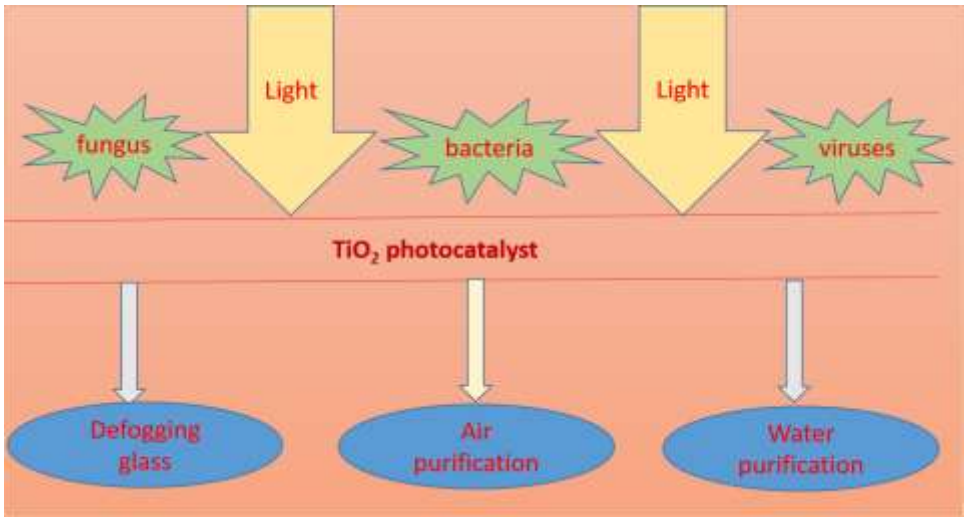

Figure1.5: Different types of photo catalysis [19].

1.7.3 Water purification: Photo catalysis plays an important role in the water purification. When the UV light falls on the photocatalyst they can oxidize the organic pollutants and mineralize it to produce nontoxic materials like CO_2 and H_2O. This process is highly effective for removing the harmful organic compounds.

1.7.4 Solar water disinfection: Solar water disinfection is also called as SODIS. It is a simple method to improve the quality of drinking water by using the photocatalyst. By using the photocatalyst or UV visible ray in sunlight, bacteria or germs can be treated/removed/killed through oxidation process.

1.8 Peroveskite Materials as a catalyst for photocatalytic reaction:

Many of the photo catalysts are peroveskite type compounds like $AgTaO_3$, $SrTiO_3$, $NaTaO_3$, $NaNbO_3$, $CaTiO_3$, $PbTiO_3$ etc. containing octahedrally co-ordinate d^0 transition metal ions. Peroveskite materials can be used as catalyst for the water splitting reactions. In a peroveskite photocatalyst, there are two main groups of elements that can be active for B site elements or cation components. The elements which includes in the first group are Ti^{4+}, Zr^{4+}, Nb^{5+} and Ta^{5+} with the empty d-orbital and elements in the second group are Sn^{4+}, Ge^{4+}, Ga^{3+} and Sb^{5+} with the filled d-orbital. The materials have also gained attention for other photocatalytic processes such as photo degradation of organic effluents due to the generation of excitons during irradiation[20]. Peroveskite has also achieved a technological interest for its potential application in Li-ion batteries, single flux quantum circuit and high temperature humidity sensor [21].

1.9 Peroveskite material (ABO_3 material)

The chemical formula for the peroveskite material is ABO_3 (where both the 'A' and 'B' atoms are considered as cations having different sizes while 'O' atom is considered as anion and 'O' bonds with both 'A' and 'B'). $BaTiO_3$, $CaTiO_3$, and $NaNbO_3$ etc. are the typical examples of peroveskite materials [22] as shown in **Figure 1.6**. ABO_3 has an ideal cubic peroveskite structure with the space group of Pm3m. In this crystal structure (cubic unit cell) atoms 'A' occupies the corner position, atom 'B' occupies the body centered position and 'O' (oxygen) atom occupies the face centered position. They have large number of crystal phase transitions and the sequence of phase transitions is: orthogonal, rhombohedral, tetragonal monoclinic and triclinic.

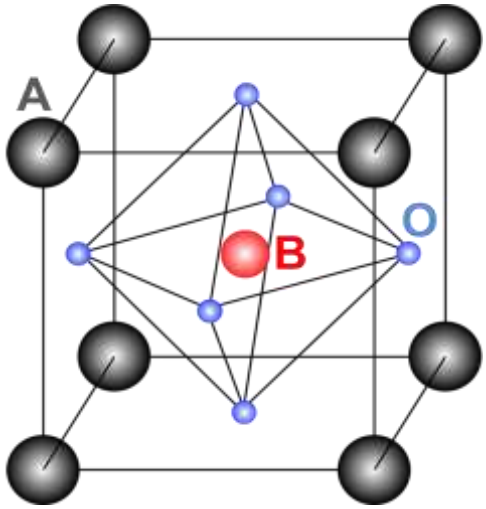

Figure 1.6: Representation of an ABO_3 peroveskite unit cell [23].

Both the cations 'A' and 'B' are situated in the 12 and 6 (respectively) coordinated symmetry with the anion i.e. 'O' atoms. With the 'A' cation, BO_6 octahedra share corners that are located in the 12-coordinated interstices sites as shown in **Figure 1.7**. The cation atoms 'A' are composed of lanthanide ions, alkaline and alkaline earth metals, whereas the cation of atom 'B' are composed of only the transition metal ions. For ABO_3 structure, halide peroveskite structure, divalent and monovalent cations are stabilized in the 'A' and 'B' sites. Substitution of both the atoms 'A' and 'B' can alter the symmetry and the composition of the peroveskite structure. The substitution can also create the cation vacancies that can affect the photocatalytic behavior and the band structure of these materials. ABO_3 peroveskite possesses large number of properties like ferroelectricity, superconductivity, antiferroelecricity, magnetism etc [21].

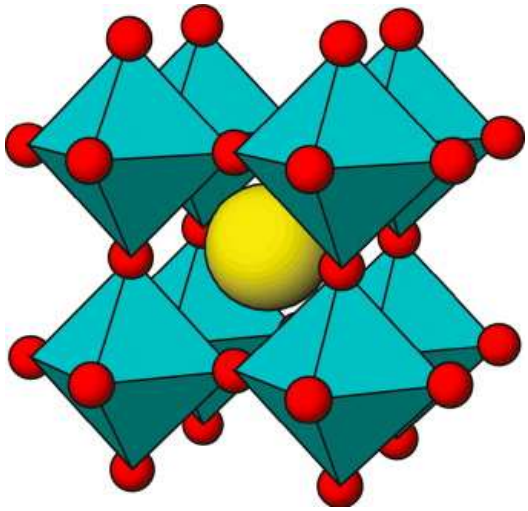

Figure 1.7: Corners sharing BO_6 octahedra with the A ion located in the 12-coordinated Interstices [24].

1.10 Advantages of $NaNbO_3$ over the other peroveskite materials for photocatalytic applications:

Among all the explored semiconducting photocatalysts, $NaNbO_3$ compound has its attractive physical properties such as high sound velocity with low density, moreover, it also exhibits paraelectric, ferroelectric and piezoelectric behavior. Nowadays, $NaNbO_3$ is considered as better catalyst to treat organic pollutants. For the H_2 generation, many researches have proved that $NaNbO_3$ is a highly efficient photocatalyst than other peroveskite materials [25].

1.10.1 Introduction of $NaNbO_3$

In 1949, Matthias [26] discovered the chemical formula $NaNbO_3$ (sodium niobate). It is an oxygen peroveskite with the largest number of phase transitions [27]. Its electronic properties and the crystal structure have not been completely understood. It has wide applications in the field of academic and industrial research such as organic pollution degradation, water splitting and CO_2 reduction. Sodium niobate has wide band gap (E_g) to the tune of 3.4 eV. So it can be used as a photocatalyst using sunlight or visible light [28].

Orthorhombic $NaNbO_3$ is an important source for lead free piezoelectric and ferroelectric materials because of its environmental friendly character and non-centro symmetric crystal structure along with non- linear optical properties [26]. The space group of monoclinic ferroelectric phase is Pm which is well known to be used in lead based peroveskite sandwiched between the rhombohedra and tetragonal ferroelectric phases and is very near to the morphotropic phase boundary [29]. The sequence of the phase transitions is still not certain. Darlington and Knight [30] have shown that

by using high resolution neutron scattering at the room temperature, the symmetry of phase P (anti-ferroelectric) should be monoclinic rather than orthorhombic. Recent study has revealed that at the low temperature, rhombohedral ferroelectric N-phase co-exist with the anti- ferroelectric orthorhombic P-phase.

At the room temperature, orthorhombic phase is the most stable phase of $NaNbO_3$ with the Pbcm space group (a = 5.506 Å, b = 5.566 Å, and c =15.52 Å) also known as antiferroelectric phase [30]. Cubic peroveskite is the most complex structure which is stable only at high temperature i.e. above 913K and is known as paraelectric phase [31]. Due to slow cooling from high temperature, there is successive phase transition i.e. cubic converted to tetragonal, then it converted into orthorhombic, followed by rhombohedral [28].

According to Megaw [32], the high temperature (above 913K) phase of $NaNbO_3$ is paraelectric as cubic peroveskite structure. Then it undergoes a phase transition from cubic to paraelectric tetragonal T (2) phase at the transition temperature of 913K with space group of F4/mmb. Then it undergoes a three distinct phase transitions into the orthorhombic phases to the paraelectric T (1) phase at the transition temperature of 848K with the space group of Ccmm, then to the paraelectric S-phase at the temperature of 793K with the space group of Pnmm and to the antiferroelectric R-phase at 753K with the space group of Pnmm. Orthorhombic R-phase undergoes a phase transition of orthorhombic P-phase with the transition temperature of 633K with the space group of Pbma. Then, final phase transition is to rhombohedral ferroelectric N-phase at the temperature of 173K with the space group of F3c. Further, all the thermal phase transitions which have been observed for $NaNbO_3$ are enlisted in **Table 1.2.**

Table 1.2: seven phases of Sodium Niobate [32].

Lattice symmetry	**Temperature (approx.)**	**Phase**	**Space group**
Rhombohedral	173K	Ferroelectric N-phase	F3c
Orthorhombic: Rhombic Orientation	633K	Antiferroelectric P-phase	Pbma
Orthorhombic: Parallel Orientation	753K	Antiferroelectric R-phase	Pnmm
Orthorhombic: Parallel Orientation	793K	Paraelectric S-phase	Pnmm
Orthorhombic: Parallel orientation	848K	Paraelectric T(1)-phase	Ccmm
Tetragonal	913K	Paraelectric T(2)-phase	F4/mmb
Cubic	above 913K	Paraelectric Arsitotype	Pm3m

References:

1. C. Descorme, Catalytic wastewater treatment: Oxidation and reduction processes. Recent Studies on chlorophenols, Catalysis today 297 (2017) 324-334.

2. L. Yu, M. Han, F. He, A review of treating oily wastewater, Arebian journal of chemistry 10 (2017) 1913-1922.

3. A. N. Angelakis, S. A. Snyder, Wastewater treatment and reuse: Past, Present, and Future, Water 7 (2015) 4887-4895.

4. M. Mittal, M. Sharma, O. P. Pandey, Fast and quick degradation properties of doped and capped ZnO nanoparticles under UV–Visible light radiations, Solar Energy 125 (2016) 51-56.

5. O. Deutschmann, H. Kneozinger, K. Kochloefl, T. Turek , Heterogeneous catalysis and solid catalysts, Ullmann's Encyclopedia of industrial Chemistry 1 (2000) 2-110.

6. C. Christophe, N. M. Schweitzer, Homogeneous and Heterogeneous catalysis: bridging the gap through surface organometallic chemistry, Angewandte Chemie International Edition 42 (2003) 156-181.

7. C. L. Copper, E. Koubek, An Experiment to Demonstrate How a Catalyst Affects the Rate of a Reaction, Journal of Chemical Education 76 (1999) 1714-1715.

8. R. Amita, S.C.Amita, Photocatalysis: Principles and Applications, vol. 2017 (2017) 1-340.

9. M. Lazar, S. Varghese, S. Nair, Photocatalytic Water Treatment by Titanium Dioxide: Recent Updates, Catalysts 2 (2012) 572–601.

10. T.S. Photocatalyst, Photocatalysis by Titania- introduction, 3 (1972) 1-28.

11. A.L.Linsebigler, G.Lu, J.T.Yates, Photocatalysis on TiO_2 surfaces: principles, mechanisms and selected results, Chemical review 95 (1995) 735-758.

12. J.C. Colmenares, R. Luque, J. M. Campelo , F. Colmenares, Z. Karpiński, A. A. Romero, Nanostructured Photocatalysts and Their Applications in the Photocatalytic Transformation of Lignocellulosic Biomass: An Overview, Materials 2 (2009) 2228-2258.

13. J. Schneider, M. Matsuoka, M. Takeuchi, J. Zhang, Y. Horiuchi, M. Anpo, D. W. Bahnemann, Understanding TiO_2 Photocatalysis: Mechanisms and Materials, Chem. Rev. 114 (2014) 9919−9986.

14. G. F. Fine, L. M. Cavanagh, A. Afonja, R. Binions, Metal oxide semi-conductor gas sensors in environmental monitoring, Sensors 10 (2010) 5469-5502.

15. M. Mittal, M .Sharma, O.P.Pandey, UV–Visible light induced photocatalytic studies of Cu doped ZnO nanoparticles prepared by co-precipitation method, Solar Energy 110 (2014) 386–397.

16. A. Kudo, Y. Misek, Heterogeneous photocatalyst materials for water splitting, Chem. Soc. Rev 38 (2009) 253-278.

17. E. F. Osterloh, Photocatalysis versus Photosynthesis: A Sensitivity Analysis of Devices for Solar Energy Conversion and Chemical Transformations, ACS Energy 2 (2017) 445-453.

18. H. Haneda, K. Data, Current status and foresight of photocatalysis, Science and technology trends 7 (2013) 67-79.

19. K. Nakata, A. Fujishima, TiO_2 photocatalysis: Design and applications, Journal of photochemistry and photobiology 13 (2012) 169-189.

20. W.Wang, M.O.Tade, Z.Shao, Research progress of peroveskite materials in Photocatalysis- and photovoltaic-related energy conversion and environmental treatment, Chem. Soc. 44 (2015) 5371-5408.

21. T. Alammar, I. Hamm, V. Grasmik, M. Wark, A. Mudring, Microwave-Assisted Synthesis of Peroveskite $SrSnO_3$ Nanocrystals in Ionic Liquids for Photocatalytic Applications, Inorg. Chem .56 (2017) 6920−6932.

22. R. S. Roth, Classification of Peroveskite and Other $AB0_3$-Type Compounds, Journal of Research of the National Bureau of Standards 58 (1957) 75-88.

23. F.A. Rabuffetti, R. L. Brutchey, Complex peroveskite oxide nanocrystals: low temperature synthesis and crystal structure, The Royal Society of Chemistry 43 (2014) 14499–14513.

24. J. Shi, L. Guo, ABO_3-based photocatalysts for water splitting, Materials International 22 (2012) 592–615.

25. E.S. Baeissa, Photocatalytic degradation of malachite green dye using $Au/NaNbO_3$ nanoparticles, Journal of alloys and components 672 (2016) 564-570.

26. M.V.laxmi, S.U.Devi, Physical Properties of Sodium Niobate ($NaNbO_3$) At Nano Structure, International Journal of Engineering Research and Development 5 (2012) 47-51.

27. Y. Hsiao, Y. Chang, T. Fang, Y. Chai, G. Chen, T. Huang, Growth and characterization of $NaNbO_3$ synthesized using reaction-sintering method, Material science and engineering 136 (2007) 129–133.

28. L. Peng, S. Ouyang, G. Xi, T. Kako, J. Ye, The Effects of Crystal Structure and Electronic Structure on Photocatalytic H_2 Evolution and CO_2 Reduction over Two Phases of Peroveskite -Structured $NaNbO_3$, The Journal of Physical Chemistry 116 (2012) 7621-7628.

29. W. Ge, Y. Ren, J. Zhang, C. P. Devreugd, J. Li, D. Viehland, A monoclinic-tetragonal ferroelectric phase transition in lead-free $(K0.5Na0.5)NbO_3$- x%$LiNbO_3$ solid solution, Journal of Applied Physics 111 (2012) 103503 (1-6).

30. R. Machado, M. Sepliarsky, M.G. Stachiotti, Relative phase stability and lattice dynamics of $NaNbO_3$ from first-principles calculations, Phys. Rev. B. 84 (2011) 1-20

31. S. Chakraborty , B. K. Sarkar , S. K. Ghosh , G. C. Das ,S. Mukherjee, Phase evolution, morphology and photo-degradation kinetics of hydrothermally synthesized tetragonal sodium niobate, J Aust Ceram Soc 53 (2017) 687-699.

32. H.D. Megaw, The seven phases of sodium niobate, Gordon and Breach Science 7 (1974) 87-89.

2. Literature Review

Among all the known peroveskite ABO_3 structures, $NaNbO_3$ holds special importance due to its excellent photocatalytic applications like dye degradation, CO_2 conversion and hydrogen production. It also exhibits for ferroelectric and piezoelectric properties. $NaNbO_3$ compound was discovered as early as in the 1949 by Matthias [1]. $NaNbO_3$ can be prepared by several methods viz. hydrothermal method (HT), solid state reaction (SSR) and polymerized complex (PC) method. Some of the important developments in last two decades on the formation of $NaNbO_3$ are being discussed as follows:

Nobre *et al.* (1996) [2] prepared ultra-fine $NaNbO_3$ particles via polymeric precursors in which they used niobium ammonia oxalate, $NH_4H_2[NbO-(C_2O_4)_3].3H_2O$, $NaNO_3$ as precursors to obtain $NaNbO_3$ with the molar ratio of Nb/Na =1. XRD confirmed that there was no intermediate phase at low temperature i.e.500˚C at which $NaNbO_3$ got nucleated and formed amorphous precursor. After the calcination at 700˚C for 5h, high crystallinity and high surface area were observed from XRD pattern and N_2 adsorption/desorption curve. Powders showed that with increase in calcination temperature, unit cell volume decreases that might be associated to the elimination of defects during thermal treatment. After sintering at 1190˚C, powder (calcined at 800˚C) reached density above 98% indicating high sinter ability. Higher surface area was obtained with calcination temperature between 600-800˚C for 5h duration, whereas reduction in surface area was reported for calcination temperature higher than 800˚C.

Camargo *et al.* (2002) [3] prepared sodium niobate by using water soluble niobium-malic acid 00gcomplex and sodium carbonate via amorphous complex method. DL-Malic acid (MA) was used as a chelating agent to reduce the amount of carbon in the (Nb-MA-Na) precursor. The solution of water soluble Nb: Na (2:1) was calcined at the temperature range of 400-900˚C for 1h. The phase formation, morphology and optical properties of a synthesized nanoparticles were studied by using XRD, SEM and UV-Raman spectroscopy. Formation of $NaNbO_3$ phase was initiated at 450˚C but pure single phase was obtained at 550˚C with average particle size of ~100nm. The elimination of residual carbon was determined by UV-Raman spectroscopy at the temperature up to 550˚C by observing the disappearance of bands at 1340 and 1587 cm^{-1}.

Goha *et al.* (2003) [4] synthesized $KNbO_3$ and $NaNbO_3$ powders via hydrothermal method at 200 ˚C using NaOH/KOH and Nb_2O_5 powders. Orthorhombic $NaNbO_3$ phase was confirmed at the

temperature range of 150-200˚C. Before they converts into the peroveskite phase, firstly intermediate hexaniobate was formed. For the synthesis of potassium hydroxide, the concentration and temperature of KOH is decreasing which increases the stability of hexaniobate ion. As per the synthesized $KNbO_3$ powder, protons were incorporated in the lattice as a water molecules and hydroxyl ions.

Hsiao *et al.* (2007) [5] followed reaction sintering method without using calcination for the synthesis of $NaNbO_3$ in which Na_2CO_3 and Nb_2O_5 were used. The mixture was milled together in acetone for 24h and dried in oven at 240˚C for 24h. Then the pellets were sintered in alumina crucible at the temperature of 1100-1200˚C for 3and 6h. XRD confirmed the formation of pure orthorhombic $NaNbO_3$ at these temperatures. For 3h and 6h the activation energy of grain growth were 86.85 and 90.58kJ/mol. At the temperature of 1200˚C, the maximum linear shrinkage was 22.9% and minimum porosity percentage of $NaNbO_3$ was 1.6% for 6h of holding and at the same temperature for 3h, $NaNbO_3$ found rhomb shaped grain with the well-defined edges.

Guoqiang *et al.* (2008) [6] synthesized $NaNbO_3$ by using SSR method, HT method and PC methods. All the prepared samples were analyzed by X-ray diffraction (XRD), scanning electron microscopy (SEM) and absorbance spectroscopy to observe the crystal structure, morphology and optical band gap, respectively. XRD confirmed that crystallinity of PC-600 is not as good as that of SSR and HT. SEM micrographs confirmed that particle size of PC method (400nm) was smaller than that of HT and SSR i.e. 700nm. Photocatalytic activity was also evaluated by H_2 evolution from an aqueous methanol solution in the presence of the Pt (0.5wt %) /$NaNbO_3$ and pure water splitting in the presence of the RuO_2 (1.25wt %) /$NaNbO_3$ respectively. According to both the reactions, PC method with the smallest particle size have highest photocatalytic activity. It showed that apart from morphology particle size plays an important role for finding the water splitting property of $NaNbO_3$.

Ke *et al.* (2008) [7] synthesized $NaNbO_3$ nanowires and cubes by using the simple base treatment of 10M Nb_2O_5 and 12.5M of NaOH solution. SEM micrographs confirmed the formation of $NaNbO_3$ nanowires with the uniform diameter of 100 nm and length of several hundred to micron. Moreover, SAED confirmed the single crystalline nature and the interplaner distance were measured to be 3.83 and 2.93Å by using HRTEM image. The piezoelectricity of single $NaNbO_3$ with the space group of Pbma nanowires was achieved by piezoresponse force microscopy.

Nanowires were heated to 400˚C yielding the orthorhombic $NaNbO_3$ and by increasing the 12.5M concentration of NaOH solution, cubes of orthorhombic $NaNbO_3$ were obtained. There was a phase transition from orthorhombic to tetragonal by the heating of sodium niobate cubes or nanowires.

Liu *et al.* (2009) [8] synthesized single crystal of sodium niobate by using the temperature induced solid phase oriented rearrangement. $Na_2Nb_2O_6.H_2O$ was used as Nb source that belongs to the Sandia octahedral molecular sieves (SOMS) family and NaOH was used as Na source. By using thermal decomposition treatment, wire like $Na_2Nb_2O_6.H_2O$ converted into $NaNbO_3$ nanowires without any morphological change. SEM and TEM were used to examine the morphological features of as synthesized $Na_2Nb_2O_6.H_2O$ precursor and $NaNbO_3$ nanowires. The morphology of the synthesized sample has wire like structure. FESEM image showed that diameter of precursors nanowires was 80nm whereas reduction in the diameter i.e. 60nm was reported after the calcination of $Na_2Nb_2O_6.H_2O$ nanowire. Single crystalline nature of $NaNbO_3$ nanowires confirmed through SAED pattern and HRTEM image of $NaNbO_3$ nanowires.

Yang *et al*. (2009) [9] synthesized pure $NaNbO_3$ powder via combustion method using Na_2CO_3 as a sodium source, Nb_2O_5 as a niobium source and urea as a fuel. Urea plays an important role to improve the efficiency in the solid state reaction. Molar ratio of sodium and niobium was [Na]/ [Nb] =1:1. Powders were mixed by wet ball milling for 4h and the mixture was dried at 80˚C in an oven for 4h. Then the precursor was placed in alumina crucible and calcined at a different temperatures from 500-700˚C. The phase composition and morphology were examined using XRD and SEM. At 500˚C, apart from the $NaNbO_3$ phase, Nb rich ($Na_2Nb_4O_{11}$) phase were also detected but with the increasing temperature i.e. 550˚C Nb rich phase disappears and pure single phase $NaNbO_3$ was obtained. SEM micrographs confirmed that cuboid like grain morphology was obtained at the temperature of 650˚C with the diameter of 300-500nm.

Shi *et al*. (2009) [10] synthesized $NaNbO_3$ nanowires and cubes via P123 assisted-hydrothermal process by taking 5g of Nb $(OC_2H_5)_5$ and NaOH as a precursor in a Teflon lined autoclave at 200˚C for 24 h. The powder was washed several times with the distilled water and dried in oven at 70˚C overnight then calcined at 550˚C for 4h. SEM morphology confirmed the formation of nanowires, in which length of nanowires up to several tens of micrometer and 100 nanometer wide. Single crystalline nature of $NaNbO_3$ nanowires was confirmed by HRTEM and SAED. Using solid state reaction method, $NaNbO_3$ synthesized having different morphology like cube, particles of different

shape, the nanowires have shown highest photocatalytic activity for the H_2 production from CH_3OH/H_2O solution under UV light radiation. In the photocatalytic activity, H_2 evolution of $NaNbO_3$ nanowires observed was 39.4% at the wavelength of 300nm.

Chaiyo *et al.* (2010) [11] synthesized Pb free piezoelectric $NaNbO_3$ via solid state reaction by using sodium oxalate ($Na_2C_2O_4$) and niobium oxide (Nb_2O_5) as a precursor. Both these materials were mixed together using the ball mill in the ethyl alcohol for 18h. The milled powder were heat treated and then thermal behavior was identified by TGA (Thermo Gravimetric Analysis) and DTA (Differential thermal analysis). The phase formation were studied by XRD confirming the formation of $NaNbO_3$ at a low temperature of 475˚C for 1h with crystallite size 31.45±5.28nm. XRD peaks become narrower with the increasing dwell time. SEM image showed the particle size of $NaNbO_3$ powders ranges from 180 to 360nm. TG curve suggested that weight loss of 16.8% were shown when the temperature increases from 400-500 ˚C and DTA curve showed endothermic peak which cantered at 484.4 ˚C.

Ji *et al.* (2010) [12] synthesized $NaNbO_3$ microcrystal with different cuboid morphology by a simple hydrothermal process with the two different bidentate organics including EDA and glycol and Nb is used a raw material. To prepare $NaNbO_3$, mixture of niobic acid and sodium hydroxide was charged to the autoclave and maintained at 180-200˚C for 2-4 days. The phase structure and morphology were investigated by using XRD and SEM. Pure orthorhombic phase of $NaNbO_3$ was confirmed by using XRD technique. Synthesis done using different amount of glycol (i.e. 15ml, 10ml, and 5ml) and EDA (i.e. 20ml, 10ml) with an NaOH aqueous solution exhibited, different cuboid based morphologies such as truncated cuboids, cuboids, vertex concaved cuboids having different size. For $NaNbO_3$, both the EDA and glycol differ from each other as on the specific surfaces owing two amino groups on the EDA whereas two hydroxyl groups at the end of glycol molecule.

Pan *et al.* (2011) [13] synthesized $NaNbO_3$ powder via hydrothermal (HT) method and conventional solid state methods. For hydrothermal method, they took sodium hydroxide and niobium oxide as a precursor into an autoclave made of stainless steel. But for the conventional solid state method, $NaNbO_3$ was synthesized by mixing the Na_2CO_3 and Nb_2O_5 in a ball mill for 12h and then heated at 1000˚C for 9h. The morphology, microstructure and phase structure were investigated by using SEM, Raman spectra and XRD. For $NaNbO_3$ ceramic, their electrical and

piezoelectric properties were also measured. By using HT method, smaller size with high crystallinity was obtained for the $NaNbO_3$ powder. Sintering temperature of the hydrothermal method was lower but compactness and electrical properties were better than that of conventional method that had orthorhombic phase structure. SEM microstructure confirmed that particles of $NaNbO_3$ was irregular and uneven with average grain size of 8µm.

Zielinska *et al.* (2011) [14] synthesized metal (Fe, Ni, Co, Ag) loaded $NaNbO_3$ via impregnation method in an aqueous solution of metal nitrate by using Nb_2O_5 and NaOH as a precursor to the molar ratio of [Nb/Na]=2:1. The samples were dried in an oven at 70˚C for 24h and then the dried sample were calcined at the temperature of 550˚C. The crystallographic phases, morphology, band gap and chemical composition of metal loaded $NaNbO_3$ were studied using XRD, HR-TEM, DR-UV- visible absorbance spectroscopy and EDX. HR-TEM confirmed that the morphology of all the investigated samples were similar and they showed high crystallinity. EDX spectrum exhibited that copper, niobium, sodium and oxygen were the only elements that present in the $NaNbO_3$ sample. By using DR-UV- visible absorbance spectroscopy the estimated band gap of $NaNbO_3$ and Nb_2O_5 was 3.34 and 3.07eV, respectively. Photocatalytic activity of $NaNbO_3$ were investigated by the photocatalytic H_2 generation. Experimental results showed that among all these metal loaded $NaNbO_3$, Ag-loaded $NaNbO_3$ showed higher photocatalytic efficiency for H_2 generation as compare to the bare $NaNbO_3$.

Kumada *et al.* (2011) [15] synthesized $NaNbO_3$ via hydrothermal reaction Nb_2O_5, a-Nb_2O_5, $HNbO_3.nH_2O$, $HNb_3O_8.nH_2O$ as Nb source and NaOH as a Na Source (1.0M). a- Nb_2O_5 precursor was obtained by reacting Nb_2O_5 and K_2CO_3 at 980˚C for 1h. Single phase of $NaNbO_3$ was obtained at the temperature of 160˚C. They have suggested the effect of starting compound on the structural feature of final product i.e. $NaNbO_3$. Basically all four precursors resulted to cubic shaped particles with different average particle sizes: 0.5, 1.0, 1-5 and 5-10µm from Nb_2O_5, $HNbO_3.nH_2O$, $HNb_3O_8.nH_2O$, a-Nb_2O_5. The particle prepared from $HNb_3O_8.nH_2O$ had cubic like shape and $HNbO_3.nH_2O$ had irregular shape but Nb_2O_5 had submicron particle size. Among all the niobium sources amorphous hydrate niobium oxide (a-NbO_5) well exhibited crystalline particles and their morphology were also different than that of ($HNbO_3.nH_2O$, $HNb_3O_8.nH_2O$ and Nb_2O_5). XRD confirmed that diffraction peaks of these three ($HNbO_3.nH_2O$, $HNb_3O_8.nH_2O$ and Nb_2O_5) starting compounds have shown broadening than that of a-Nb_2O_5.

Li *et al.* (2012) [16] synthesized cubic and orthorhombic $NaNbO_3$ to study the effect of crystal structure and electronic structure on the photocatalytic H_2 evolution and CO_2 reduction, by using two different sets of compounds $(C_2H_5O)_5$ Nb and C_2H_5ONa $NbCl_5$ and Na_2CO_3 and $NbCl_5$. Both the phases of peroveskite structure of $NaNbO_3$ was synthesized via furfural alcohol derived polymerization oxidation process (FAPO) and polymerized complex (PC) method. Crystal structure and morphology were determined using the XRD and HRTEM. Cubic-$NaNbO_3$ showed higher activity in photocatalytic H_2 evolution (~1000µmole) than that of Orthorhombic $NaNbO_3$ (800µmole) by virtue of narrower band gap of cubic phase than orthorhombic $NaNbO_3$. Higher activity of Cubic $NaNbO_3$ can be attributed for its electronic structure which is suitable for electron excitation and transfer phenomenon. By using the Debye Scherer formula crystallite size of cubic and orthorhombic $NaNbO_3$ was determined which came out to be 18.5nm and 23.1nm, respectively. TEM and HRTEM confirmed that cubic- $NaNbO_3$ shows uniform cubic morphology whereas orthorhombic-$NaNbO_3$ contains irregular and cuboid particles. Moreover, CO_2 reduction ability of both the phases have also been studied. In this, evolution rate of methane, over cubic-$NaNbO_3$ become double than that of orthorhombic - $NaNbO_3$ in the gas phase of CO_2 photo reduction.

Boukriba *et.al.* (2013) [17] prepared triangular prism like of rhombohedral $NaNbO_3$ via hydrothermal process by using the mixture of Nb_2O_5 and (NaOH). Stirring the solution done for 1h at room temperature followed by heating at 180˚C for 6h in Teflon lined autoclave resulted to the formation of $NaNbO_3$. The powder were washed several times with ethanol and distilled water and then dried in oven at 60˚C. The structure and morphology were determined by using different techniques like XRD, SEM and Raman spectroscopy. Their electronic properties of $NaNbO_3$ have shown that it has a strong dependence of temperature and frequency. Arrhenius diagram of the electrical conductivity for rhombohedra $NaNbO_3$ was not linear and their corresponding activation energies was 0.893, 0.507, 0.819 and 0.105 eV as deduced from the Arrhenius relation.

Shi *et al.* (2014) [18] investigated the effect of nitrogen concentration on the electronic structure of N-doped $NaNbO_3$ using the first principles calculation. As per the doping concentration two possible mechanism for the interaction of visible light for N-doped $NaNbO_3$ has been given. These are as follows: at lower nitrogen doping concentration the localized O-2p states are formed below the N-2p states. It leads to reduction of optical excitation energy as compared to the undoped

compound. The second is higher doping nitrogen level in which O-2p states are mixed with the N-2p states resulting up shift of valance band edge. With the various N-doping levels, optical band gap of pure $NaNbO_3$ was 2.48 eV which is very less as compared to the experimental value of $NaNbO_3$ i.e. 3.4 eV. Such transitions from UV excited $NaNbO_3$ to visible active $NaNbO_3$ can open various engineering applications under solar radiation.

Gu *et al.* (2014) [19] synthesized platelike $NaNbO_3$ templates powder via one step surfactant free hydrothermal route in which they took sodium acetate, 10M potassium hydroxide, and 0.5g of niobium pentaoxide into an Teflon lined vessel. Rhombohedral structure with the width and thickness of 20µm and 2 µm were obtained at 200˚C for 16h of holding. But after the calcination temperature at 600˚C for 4h, there was phase transition from rhombohedral to orthorhombic and hence platelike morphology was obtained. No other elements than Nb, Na and oxygen were obtained in the chemical composition (observed from EDS spectra) of as synthesized platelike $NaNbO_3$ templates. At the higher temperature, platelike $NaNbO_3$ templates shows morphological othorhombic structure and it also shows thermal stability.

Li *et al.* (2014) [20] investigated the effect of doping with Co and La on the of photocatalytic H_2 evolution response of $NaNbO_3$. Doped and undoped $NaNbO_3$ were prepared via hydrothermal method in which 1.0 g of $(C_2H_5O)_5Nb$ and 0.24 g of C_2H_5ONa were mixed and heated in an autoclave at 180˚C for 24 min and $La(CH_3COO)_3$ and $Co(CH_3COO)_2$ were used as a dopant reagent for the synthesis of doped $NaNbO_3$. SEM confirmed that the morphology of pure $NaNbO_3$ were almost similar with the doped $NaNbO_3$. As compared to the band gap of undoped $NaNbO_3$ (i.e.3.4eV), Co and La doped $NaNbO_3$ show narrower band gap. Doped $NaNbO_3$ also showed photocatalytic activity for hydrogen evolution under visible light whereas undoped $NaNbO_3$ was not active. According to the theoretical calculation, Co dopant create new state in between valance band and conduction band edge of $NaNbO_3$.

Baeissa (2016) [21] studied the $Au/NaNbO_3$ nanoparticle for the photocatalytic degradation of malachite green (MG) dye in the presence of visible light for the synthesis of $NaNbO_3$ nanoparticles. Hydrothermal temperature ranging from 100-250˚C controls the shape and the surface area of nanoparticles. Nb_2O_5, NaCl and $HAuCl_4$ used as a precursor for the preparation of $Au/NaNbO_3$. At the different temperatures, mixture was heated in an autoclave for 12h and then dried in oven at 80˚C for 24h. For the preparation of $Au/NaNbO_3$ photo assisted deposition method

was applied. Band gap of sodium niobate were decreases, when it is doped with Au but the surface area of $NaNbO_3$ was higher than that of Au/$NaNbO_3$. The photocatalytic activity of Au/$NaNbO_3$ was higher than bare $NaNbO_3$ to degrade the MG dye under the visible region.

Vlazan *et .al* (2016) [22] synthesized Pb free sodium niobate ($NaNbO_3$) using hydrothermal method in which they took ammonium niobate oxalate hydrate ($C_4H_4NNbO_9.H_2O$), Sodium citrate($C_6H_5O_7Na_3.2H_2O$) and 7M sodium niobate (NaOH) as a precursor into an autoclave made of stainless steel at 220˚C for 10h. The phase composition, morphology, band gap and chemical composition were confirmed by XRD, SEM, EDX, UV-visible spectroscopy and FTIR. XRD confirmed that cubic structure was obtained with the lattice parameter of a=b=c=3.909Å. At the temperature of 600˚C, average particle size of 2-3 micrometer with an estimated band gap i.e.3.45eV was obtained. All the elements of $NaNbO_3$ i.e. Nb, Na and oxygen was confirmed by the EDX spectra and by using FTIR spectrum Nb-O stretching, Nb-O-Nb bending and lattice vibrations were observed.

Wang *et al*. (2016) [23] synthesized the cubic $NaNbO_3$ nanoparticle with surface ligand assisted localized crystallization (SLALC) method at 350˚C to study the adsorption and photo degradation recoverability due to the abundance of surface hydroxyl group. Niobium oxalate and NaOH were used as a precursor and the mixture heated at 400-500˚C for 1-4h. As per synthesized cubic-$NaNbO_3$ nanoparticle, the adsorption efficiency of methylene blue dye was 95% in 3min and 99.3% dye was degraded in 180min. TEM and HRTEM confirmed the rice like nanoparticles with an average particle size of 27nm. As compared to the solid state reaction method, the reaction temperature of SLALC was low and as prepared white powdered cubic nanoparticles were well crystalline. EDS spectrum reported that Cu and C elements originated from the TEM cooper grid and carbon support film along with Na, Nb and O originate from powder sample.

Gua *et al.* (2017) [24] synthesized $NaNbO_3$ nanopowder (N-$NaNbO_3$) and submicron powder (M-$NaNbO_3$) via solvothermal and hydrothermal method, respectively. In which sodium hydroxide and niobium oxide were used as a precursor. Sintering activities were investigated by the solid state sintering method. The structure, morphology and elemental composition of surface were examined by using XRD, SEM and XPS, respectively. N-$NaNbO_3$ sample showed higher sintering activities and shrinkage was four times higher as compared to the submicron powder (M-$NaNbO_3$). At the temperature of 950˚C, N-$NaNbO_3$ were obtained. In the whole frequency range, sintered N-

$NaNbO_3$ showed better dielectric properties due to unique crystal structure and less oxygen vacancies. Further a high dielectric constant (~8000) was also determined for N-NaNbO3 at room temperature which was related to abnormal phase transition.

Li *et al.* (2018) [25] synthesized potassium sodium niobate (NKN) via microwave assisted hydrothermal solvothermal method by using the KOH, NaOH and Nb_2O_5 as a precursors with molar ratio of KOH/NaOH as 3:1. In the mixture of hydroxide solution appropriate amount of Nb_2O_5 was mixed and then stirred for 30 min. Powder synthesized with microwave assisted hydrothermal solvothermal method at 200˚C for 90min have fine and homogeneous grain size as compared to the conventional method. But after the calcination at 200˚C for 30min pure single phase of potassium sodium niobate was obtained. As compared to the conventional synthesis method, sintered sample obtained from opted route showed better dielectric and piezoelectric properties. Physical and electrical properties of NKN sample showed that as the sintering temperature increases from 1000˚C to 1050˚C, piezoelectric coefficient (d_{33}), electrochemical (kp), and density (ρ) were also increased.

References

1. M. laxmi, S. U. Devi, Physical Properties of Sodium Niobate ($NaNbO_3$) at Nano Structure, International Journal of Engineering Research and Development 5 (2012) 47-51.

2. M. A. L. Nobre, E. Longo, E. R. Leite, J.A. Varela, Synthesis and Sintering of Ultra-fine $NaNbO_3$ Powder by use of Polymeric Precursors, Materials Letters 28 (1996) 215-220.

3. E. R. Camargo, M. Popa, M. Kakihana, Sodium Niobate ($NaNbO_3$) Powders Synthesized by a Wet-Chemical Method Using a Water-Soluble Malic Acid Complex, Chem. Mater. 14 (2002) 2365-2368.

4. G. K. L. Goha, F. F. Lange, S. M. Haile, C. G. Levi, Hydrothermal Synthesis of $KNbO_3$ and $NaNbO_3$ Powders, J. Mater. Res. 18 (2003) 338-345.

5. Y. Hsiao, Y. Chang, T. Fang ,Y. Chai , G. Chen, T. Huang, Growth and Characterization of $NaNbO_3$ Synthesized using Reaction-Sintering Method, Materials Science and Engineering 136 (2007) 129–133.

6. L. Guoqiang, K. Tetsuya, W. Defa, Z. Zhigang, Y. Jinhua , Synthesis and Enhanced Photocatalytic Activity of $NaNbO_3$ Prepared by Hydrothermal and Polymerized Complex Methods, Journal of physics and chemistry of solids 69 (2008) 2487-2491.

7. T. Ke, H. Chen, H. Sheu, J. Yeh, He. Lin, C. Lee, H. Chiu, Sodium Niobate Nanowire and Its Piezoelectricity, J. Phys. Chem. *C* 112 (2008) 8827–8831.

8. L. Liu, B. Yu, Y. Cui, X. Zhou, W. Ding, Temperature-Induced Solid-Phase Oriented Rearrangement Route to the Fabrication of $NaNbO_3$ Nanowires, Chem. Commun 46 (2009) 427–429.

9. H. Yang, Y. Lin, J. Zhu, F. Wang, Low-Temperature Combustion Synthesis of $NaNbO_3$ Powders, Materials and Manufacturing Processes 24 (2009) 550-553.

10. H. Shi, X. Li, D. Wang, Y. Yua, Z. Zou, Jinhua Ye, $NaNbO_3$ Nanostructures: Facile Synthesis, Characterization, and Their Photocatalytic Properties, Catal Lett 132 (2009) 205–212.

11. N. Chaiyo, B. Boonchom, N. Vittayakorn, Solid-State Reaction Synthesis of Sodium Niobate ($NaNbO_3$) Powder at low Temperature, J Mater Sci 45 (2010) 1443–1447.

12. L. Ji, M. Liu, D. Xue, Polymorphology of Sodium Niobate based on Two Different Bidentate organics, Materials Research Bulletin 45 (2010) 314–317.

13. H. Pan, G. Zhu, X. Chao, L. Wei, Z. Yang, Properties of $NaNbO_3$ Powders and Ceramics Prepared by Hydrothermal Reaction, Materials Chemistry and Physics 126 (2011) 183–187.

14. B. Zielinska, E. B. Palen, R. Z. Kalenczuk , Preparation, Characterization and Photocatalytic Activity of Metal Loaded $NaNbO_3$, Journal of physics and chemistry of solids 72 (2011) 117-123.

15. N. Kumada, Q. Dong, Y. Yonesaki, T. Takei, N. Kinomura, Hydrothermal synthesis of $NaNbO_3$—morphology change by starting compounds, Journal of the Ceramic Society of Japan 119 (2011) 483-485.

16. P. Li, S. Ouyang, G. Xi, T. Kako, J. Ye, The Effects of Crystal Structure and Electronic Structure on Photocatalytic H_2 Evolution and CO_2 Reduction over Two Phases of Peroveskite-Structured $NaNbO_3$, J. Phys. Chem. C 116 (2012) 7621−7628.

17. M. Boukriba, F. Sediri, N. Gharbi, Hydrothermal Synthesis and Electrical Properties of $NaNbO_3$, Materials Research Bulletin 48 (2013) 574–580.

18. H. Shi, B. Lan, C. Zhang , Z. Zou, Nitrogen Doping Concentration influence on $NaNbO_3$ from First-Principle calculations , Journal of Physics and Chemistry of Solids 75 (2014) 74–78.

19. Q. Gu, K. Zhu, J. Liu, J. Wang, P. Liu, Q. Sun, J. Qiu, One-Step Surfactant-Free Hydrothermal Synthesis of Platelike Sodium Niobate Template Powders, J. Am. Ceram. Soc. 97 (2014) 3360–3362.

20. P. Li, H. Abe, J. Ye, Band-Gap Engineering of $NaNbO_3$ for Photocatalytic H_2 Evolution with Visible Light, International General of Photo Energy Vol. 2014 (2014)1-6.

21. E.S. Baeissa, Photocatalytic Degradation of Malachite Green Dye using $Au/NaNbO_3$ nanoparticle, Journal of Alloys and Compounds 672 (2016) 564-570.

22. P. Vlazan, P.S Firloaga, F. Stefania rus, Synthesis and Characterization of lead free Sodium Niobate Powder, Studia ub chemia 2016 (2016) 33-41.

23. L. Wang, H. Gu, J. H, T. Zhao, X. Zhang, C. Xiao, H. Liu, X. Zhang, Y. Li, Scale synthesized Cubic $NaNbO_3$ Nanoparticles with recoverable Adsorption and Photo degradation for Prompt removal of Methylene Blue, Journal of Alloys and Compounds 695 (2017) 599-606.

24. Q. Gu, Q. Sun, K. Zhu, J. Liu, J. Qiu, Low-temperature Sintering and Enhanced Dielectric properties of Alkali Niobate Ceramics Prepared from Solvothermal Synthesized Nanopowder, Ceramics International 43 (2017) 1135–1144.

25. H. Li, Y. Yan, G. Wang, Q. Li, Y. Gul, J. Huang, Hydrothermal Solvothermal Synthesis Potassium Sodium Niobate lead-Free Piezoelectric Ceramics Assisted with Microwave, J Mater science: Mater electron 29 (2018) 746-752.

3. Experimental work

In the present work, undoped and Ca-doped sodium niobate ($NaNbO_3$) nanopowder were prepared through chemical precipitation route. The resource materials include ammonium niobate oxalate hydrate (ANO; $C_4H_4NNbO_9.xH_2O$, *Sigma Aldrich, 99.99%*) and sodium sulphide (SS, Na_2S, *Loba Chemie*). The materials are of analytical grade and used without further purification. ANO was used as niobium source and sodium sulphide (Na_2S) as sodium source and precipitating agent, both. The detailed description of the methodology is as follows:

3.1 Methodology

In a typical procedure, 20ml of homogeneous solution of 0.5M ANO and SS were prepared in the distilled water separately. Both these solutions were allowed to stir for 15-20 minutes. The molar concentration of sodium sulphide was varied in the ratio of ANO/SS: 1:1, 1:2, 1:5, 1:10, 1:15, 1:20 and 1:25. After stirring, SS solution was added drop-wise to the Nb solution resulting white colored precipitates. Further, the suspension solution was stirred for 1h at 80˚C. The settled precipitates were collected and washed with distilled water and ethanol several times using filter paper. Then the precipitates were dried in vacuum oven at 70˚C for 24h. Finally, the white powder obtained was subjected for calcination at different temperatures (600-800˚C) in furnace. The heating rate was kept 10˚C/min with the holding time of 5h. After calcination at desired temperatures, the furnace was allowed to cool at room temperature. The calcined samples were ground into a fine powder using pestle mortar and further used for characterizations as shown in **Figure 2.1.**

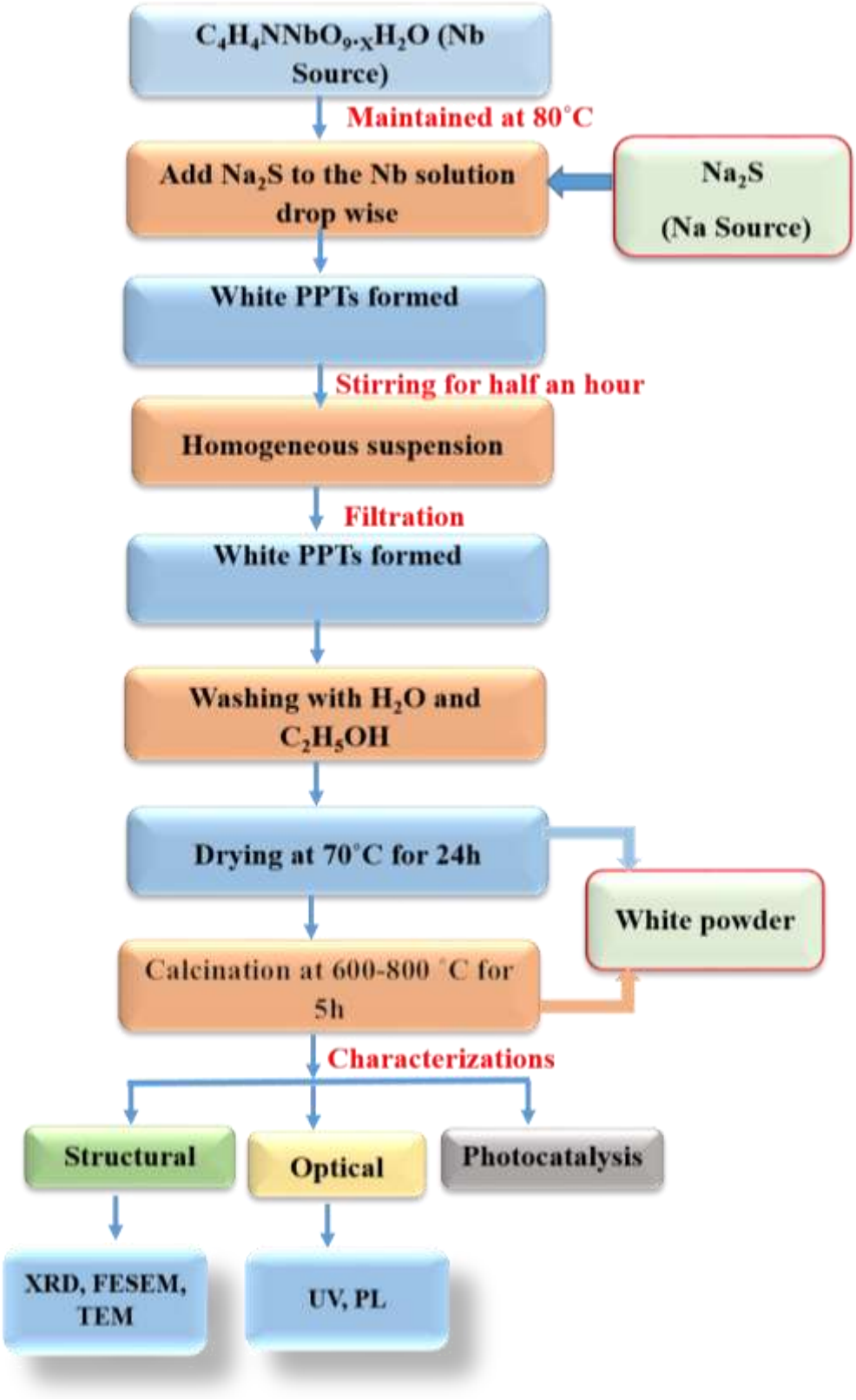

Figure 3.1: Flow chart for the synthesis of $NaNbO_3$ powder

Table 3.1: Details of the experimental condition for preparing undoped and Ca doped $NaNbO_3$.

Sample Id	Molar ratio	Dopant concentration (mole %)	Temp. (˚C)	Molar ratio	Sample Id	Dopant concentration (mole %)	Temp. (˚C)
S1	1:1	-	600	**S13**	1:15	-	800
S2	1:1	-	700	**S14**	1:20	-	700
S3	1:1	-	800	**S15**	1:20	-	800
S4	1:2	-	600	**S16**	1:25	-	700
S5	1:2	-	700	**S17**	1:25	-	800
S6	1:2	-	800	**0.5 Ca**	1:25	0.5	800
S7	1:6	-	600	**1.0 Ca**	1:25	1.0	800
S8	1:6	-	700	**1.5 Ca**	1:25	1.5	800
S9	1:6	-	800	**2.0 Ca**	1:25	2.0	800
S10	1:10	-	700	**4.0 Ca**	1:25	4.0	800
S11	1:10	-	800	**6.0 Ca**	1:25	6.0	800
S12	1:15	-	700				

3.2 Characterization

3.2.1 X-Ray diffraction (XRD)

In order to determine the crystal structure X-ray diffraction technique was used. For it Bragg's law was used. It is $2dsin\theta = n\lambda$ as shown in **Figure 3.2.** λ = wavelength of characteristic X-ray beam (λ=1.5418 Å in present case), d = interplaner distance, θ = Braggs angle, n = order of diffraction (an integers) [1].

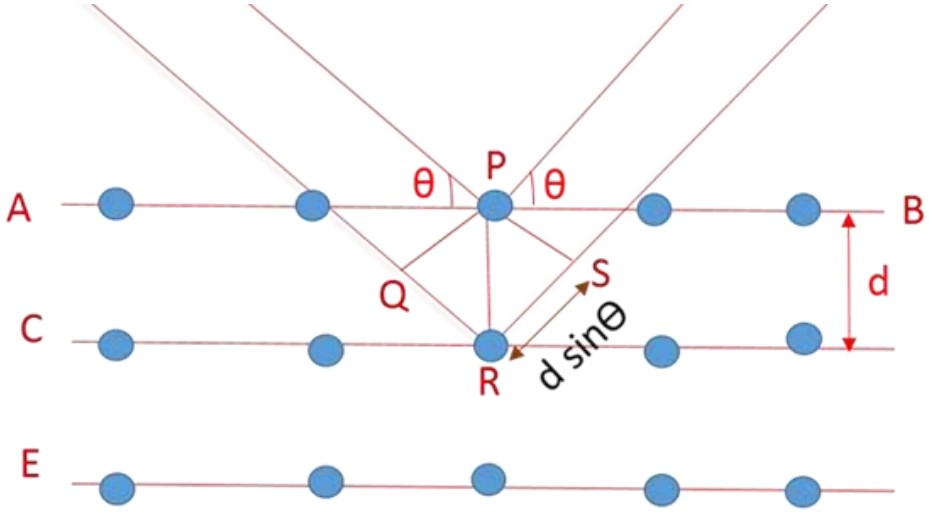

Figure 3.2 Schematic representation of the Bragg's equation

For the proposed work, XRD analysis was done on *PANanalytical* with Cu-Kα radiation with an applied voltage of 45 kV, and current range of 40 mA. 2θ range lies between 10 to 80˚ with 0.013˚ as step size. For the calculation of crystallite's size and lattice distortion, Scherer formula and uniform strain model (USM) of Williamson-Hall analysis were used which are being described as follows[2];

Scherer's formula $t = k\lambda/\beta cos\theta$ (1)

USM model $\beta cos\theta = 4\varepsilon sin\theta + (k\lambda/t)$ (2)

3.2.2 UV-Visible spectroscopy

UV-visible spectroscopy (absorption or reflectance spectroscopy) is the measurement of optical absorbance ability of samples. Absorption of the ultra-violet (UV) radiations results in the transition of the electrons from the ground state to higher energy state. For UV-visible spectroscopy, electronic excitation occurs in the range of 200-800nm. All the samples were tested in *Hitachi U3900H spectrophotometer* instrument. UV–visible spectra shows the relation between absorbance (α) and wavelength (λ) by using Tauc's plot; $\alpha h\nu = A\left(h\nu - E_g\right)^n$; where 'n' represents the type of transitions such as allowed direct (0.5), allowed indirect (2.0), forbidden indirect (1.5) and forbidden direct (3.0) transitions.

3.2.3 Transmission electron microscope (TEM)

TEM is optical instrument that uses electrons as the replacement of light to magnify the objects at a very high resolution. It is a microscopic technique whereby an electron beam is transmitted through an ultra-thin specimen (thickness less than 1µm), interacting with the sample as it passes through and corresponding image is focused at certain distance giving rise to structural features [3]. The samples were analyzed on *JEOL2100F* instrument with 200 kV operating voltage. For the sample preparation, very small amount (0.1mg) of sample was dispersed in ethanol with the help of ultrasonicator for 1h till homogenous dispersion was obtained. Then, 30µl solution was drop-casted on carbon coated Cu grid and dried overnight prior to examine under microscope.

3.2.4 Photoluminescence (PL)

Photoluminescence is a non-contact and non-destructive method to examine the optical excitation and emission characteristics of materials [4]. During the de-excitation of electron, a luminescent light particle (photon) is emitted from the material which is known as photoluminescence. The energy of the photoluminescence or emitted light correlates with the energy level difference between the two electron states that associated with the transition between the excited state and

equilibrium state. The quantity of the emitted light is related to the relative contribution of the radiative process. An excitation spectrum is very similar than that of absorption spectrum. The greater the absorbance is at the excitation wavelength, the more molecules are in excited sate and more emission will be observed. To obtain emission spectra of synthesized samples, $\lambda_{exc} = 280nm$ was chosen as excitation wavelength and photoluminiscence spectra of all the powdered sample was recorded with (Agilent Technologies- Model Cary Ellipse) equipment with Xenon lamp.

3.2.5 Field emission scanning electron microscope (FESEM)

FESEM is a technique that works with electrons instead of light in which electrons are emitted by a field emission source. FE scanning electron microscope is a very conventional tool for high resolution surface imaging in the field of nano material science. All the samples were investigated with *HITACHI SU8010* instrument at the magnification upto 180,000x.

3.2.6 Photocatalytic activity

The photocatalytic activity of as-synthesized samples was examined by using methylene blue (MB) dye as a model organic compound which is also an industrial effluent. 100ml of homogenous solution of 0.1mg MB dye was prepared in the distilled water and allowed to stir at least for 30 min. Thereafter, different amount of catalyst (200mg, 400mg and 600mg) was added in the above solution to optimize the concentration of photocatalyst for efficient performance. The prepared dye solution was kept in the dark chamber with continuous stirring for another half an hour to establish adsorption-description equilibrium. Thereafter, the solution was exposed to 80W CFL lamp for the photo degradation during 5h with an interval of 60min. At each interval, 4ml aliquot was extracted and centrifuged at 4500RPM and supernatant was examined by *Hitachi U3900H spectrophotometer* to observe the variation in absorption of MB dye at 665nm. Further, optimized concentration of undoped $NaNbO_3$ was taken for the tests done by using Ca doped $NaNbO_3$.

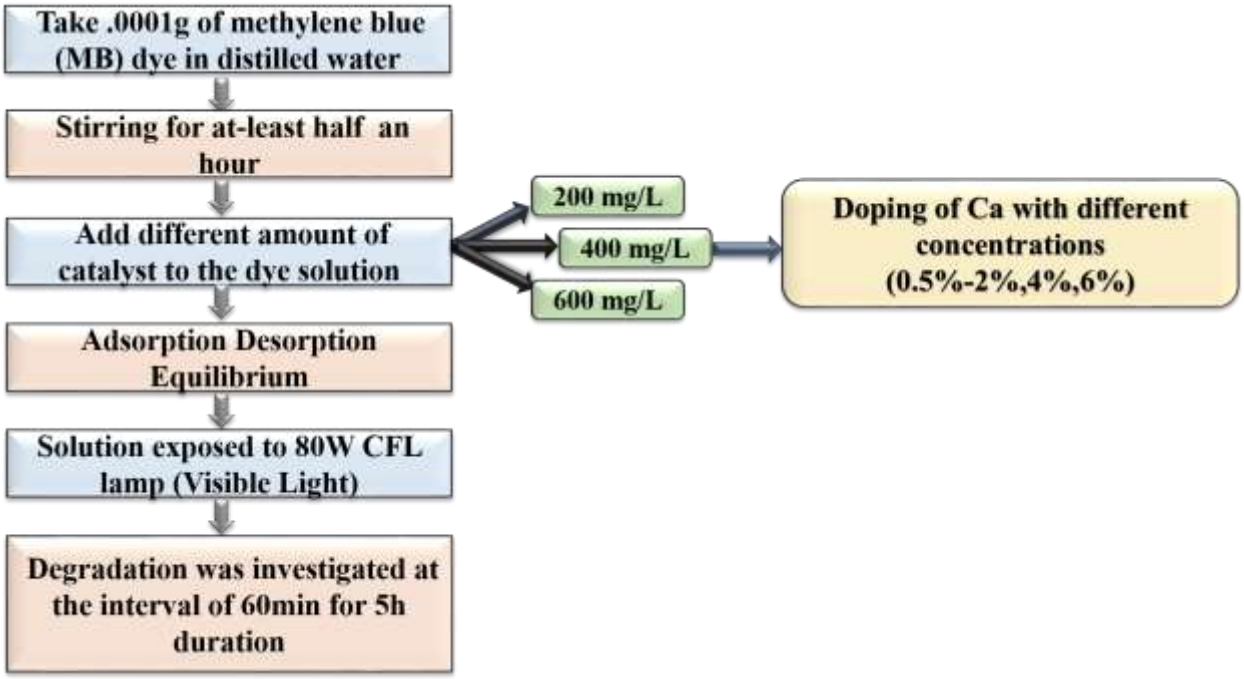

Figure 3.3: Flow chart showing photocatalytic activity for undoped and Ca doped $NaNbO_3$.

References

1. J. Kaur, Synthesis and photocatalytic studies of ZnS photo catalytic process, Thesis (2014).

2. A.Gupta, O.P. Pandey, Visible irradiation induced photo degradation by NbC/C Nano composite derived from smoked cigarette litter (filters), Solar Energy 163 (2018) 167–176.

3. N. Mittal, O. P. Pandey, Synthesis and photocatalytic studies of ZnO nanoparticles, Thesis Diss.(2010) .

4. H. Khan, Synthesis, Characterization and Photocatalytic Activity of Titanium Dioxide (Pure and Doped) Photocatalyst for the Degradation of Aqueous Organic Pollutants, thesis (2015).

4. Results and discussion

In the proposed work, nano-crystalline $NaNbO_3$ has been obtained through 2-step method i.e. chemical route followed by heat treatment at different temperatures (600, 700 and 800°C). Further, effect of Ca doping on structure, optical and catalytic properties of $NaNbO_3$ has been discussed in this chapter.

4.1 XRD analysis:

4.1.1 Preparation of undoped $NaNbO_3$: Because of chemical reaction and post-heat treatment, samples were characterized by X-ray diffraction to determine the structural features and sample composition of as-synthesized powder samples. All the diffraction peaks were analyzed and matched with ICDD cards [1] which have been listed in **Table 4.1**. As a result of chemical reaction between ANO and SS, white colored PPTs were obtained which has been characterized by XRD as shown in **Figure 4.1** confirming the amorphous nature of PPTs by two broad humps at 20-40° and 40-60.

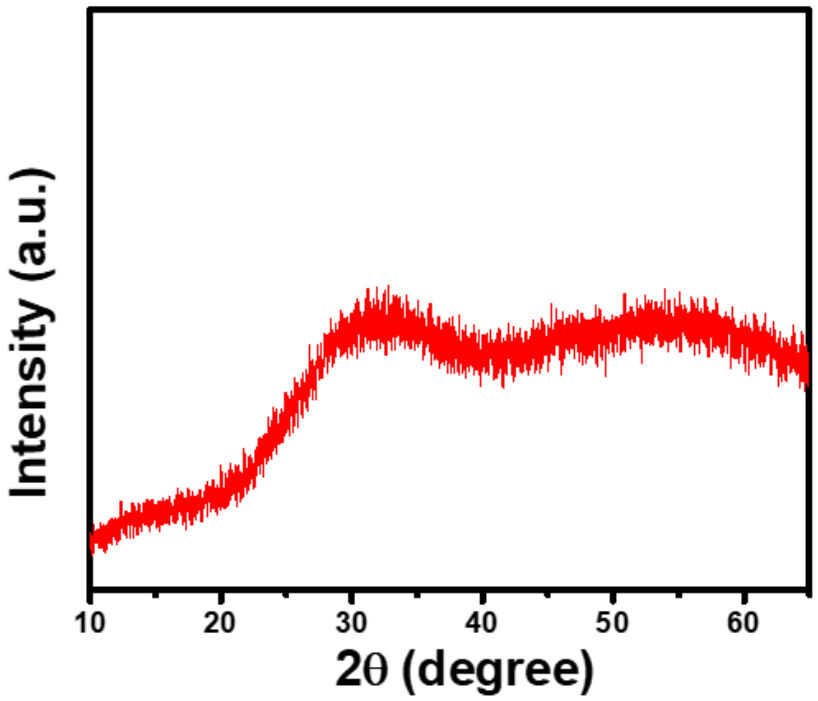

Figure 4.1: XRD pattern of white colored PPTs obtained from chemical reaction between ANO and SS.

Table 4.1: List of standard ICDD cards with the proposed work.

S. No.	ICDD card	Phase	Crystal structure
1.	01-073-0803	$NaNbO_3$	Orthogonal
2.	01-072-1694	$Na_2Nb_4O_{11}$	Monoclinic
3.	01-070-2005	$Na_3Nb_4O_{11}$	Monoclinic

Further, the dried PPTs were charged to furnace at different temperatures for 5h holding time. **Figure 4.2** represents the XRD patterns of samples (S1, S4, S7), (S2, S5, S8) and (S3, S6, S9) treated at 600, 700 and 800˚C, respectively. It can be seen from the XRD patterns (S1-S9) that molar ratio played a vital role in the formation of $NaNbO_3$. In the XRD spectra, it was observed that heat treated powder consisted of O-$NaNbO_3$ (orthogonal) and M-$Na_2Nb_4O_{11}$ (monoclinic). In the beginning, when the sample was heated at the different temperatures i.e. 600, 700 and 800˚C for 5h (S1, S2 and S3, respectively) with the molar ratio (Nb:Na) of 1:1, all the peaks corresponding to O-$NaNbO_3$ and M-$Na_2Nb_4O_{11}$ phases[2] as shown in **Figure 4.2a** were observed. Ratio of both these phases is almost same. No significant change in the XRD pattern at each temperature with molar ratio of 1:1 was observed. However, when the sample was heated at the same temperatures for 5h with the molar ratio of 1:2 (S4, S5, S6) as shown in **Figure 4.2b**, there was an increment in the volume fraction of O-$NaNbO_3$ in the mixture of O-$NaNbO_3$ and M-$Na_2Nb_4O_{11}$. Further increase in the molar ratio from 1:2 to 1:5 (S7, S8, S9) resulted in large increment in the volume fraction of O-$NaNbO_3$ from 600 to 700˚C as shown in **Figure 4.2c**. While, increased temperature from 700 to 800 ˚C did not affect the sample composition significantly. All the above observations suggested that there is insufficient Na to attach with Nb-O network to obtain single phase $NaNbO_3$ indicating the role of Na^+ ion during the final product formation while performing heat treatment. Moreover, increased molar ratio confirmed the attachment of Na^+ to M-$Na_2Nb_4O_{11}$ resulting O-$NaNbO_3$.

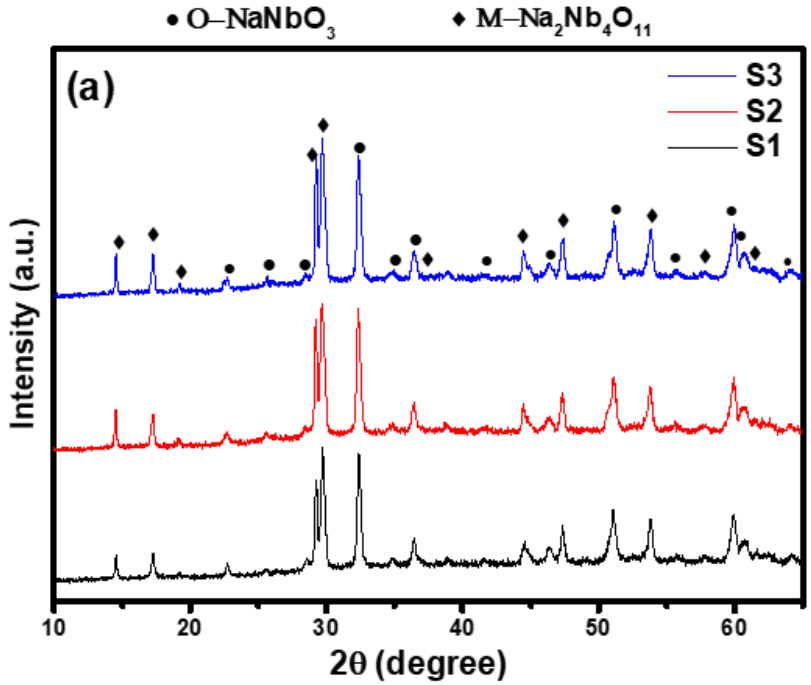
• O–NaNbO3
♦ M–Na2Nb4O11
(a)
S3
S2
S1
Intensity (a.u.)
10
20
30
40
50
60
2θ (degree)

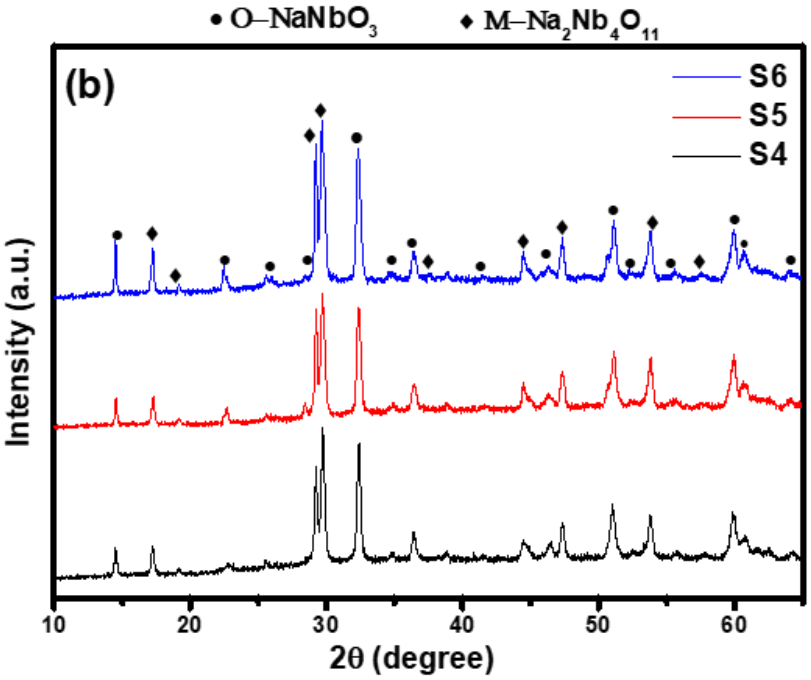
• O–NaNbO3
♦ M–Na2Nb4O11
(b)
S6
S5
S4
Intensity (a.u.)
10
20
30
40
50
60
2θ (degree)

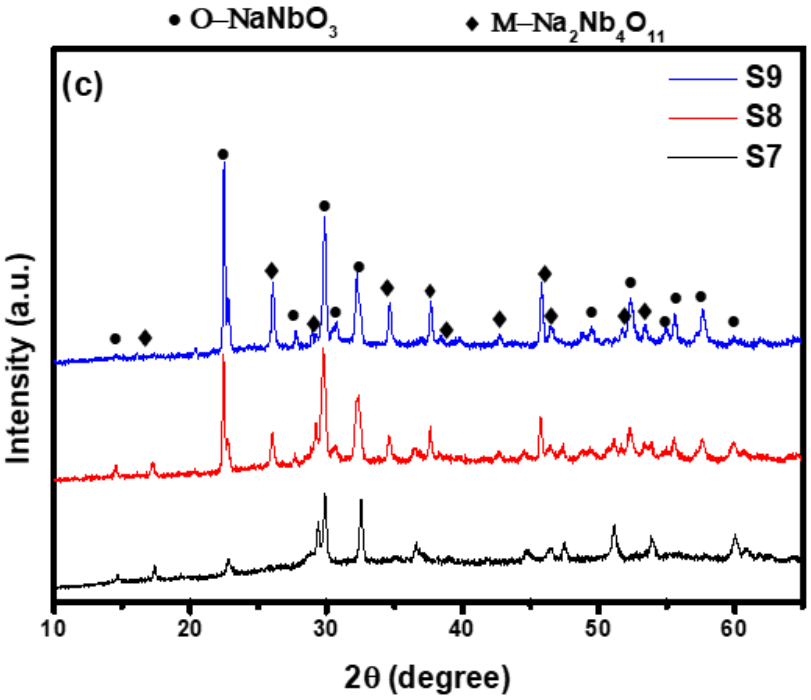

Figure 4.2: Effect of molar ratio at different temperature for 5h.

Figure 4.3 shows the XRD patterns of the samples S10, S12, S14, S16 (heat treated at 700°C) and S11, S13, S15, S17 (heat treated at 800°C) synthesized with different molar ratios (as listed in **Table 2.1**) with the holding time of 5h in which O-$NaNbO_3$ (orthogonal), M-$Na_2Nb_4O_{11}$ (monoclinic) and M-Na_3NbO_4 (monoclinic) phases were obtained. As a result of increasing molar concentration of Na up to 1:15 (Nb: Na), the formation of $NaNbO_3$ has increased at both the temperatures (700 and 800°C) as shown in **Figure 4.3a**. While, molar ratio 1:20 (Nb:Na) resulted to a new intermediate compound which is supposed to be Nb deficient system along with O-$NaNbO_3$ and further increment in molar ration (1:25) incorporate single phase of $NaNbO_3$ at 700 and 800˚C as shown in **Figure 4.3b** (sample S16 and S17). Though, S16 and S17 consisted single phase $NaNbO_3$, diffraction peaks of S17 showed lesser peak shifting when compared with ICDD card. Therefore, the synthesis conditions were kept similar to study the doping of Ca in $NaNbO_3$ which has been discussed in following sub-section.

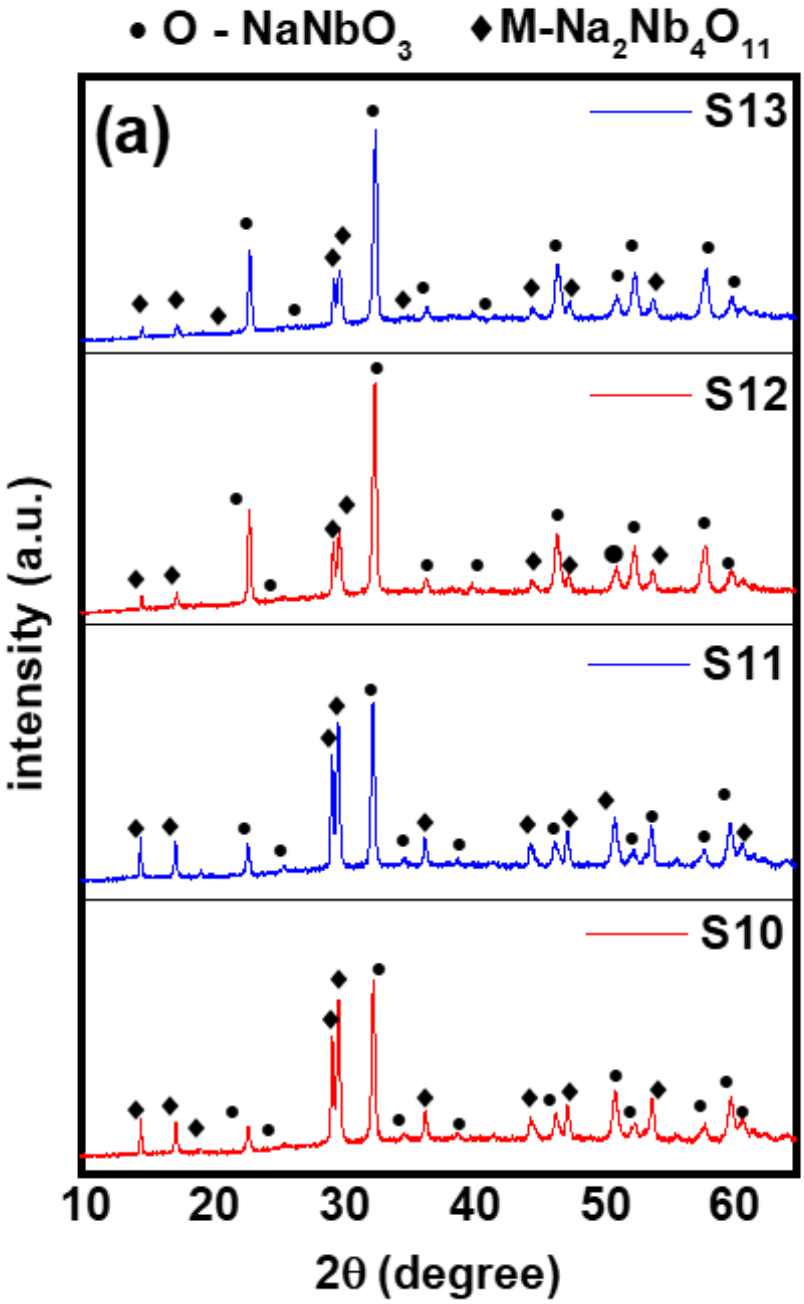
• O - NaNbO3
♦M-Na2Nb4O11
(a)
S13
S12
S11
S10
intensity (a.u.)
10
20
30
40
50
60
2θ (degree)

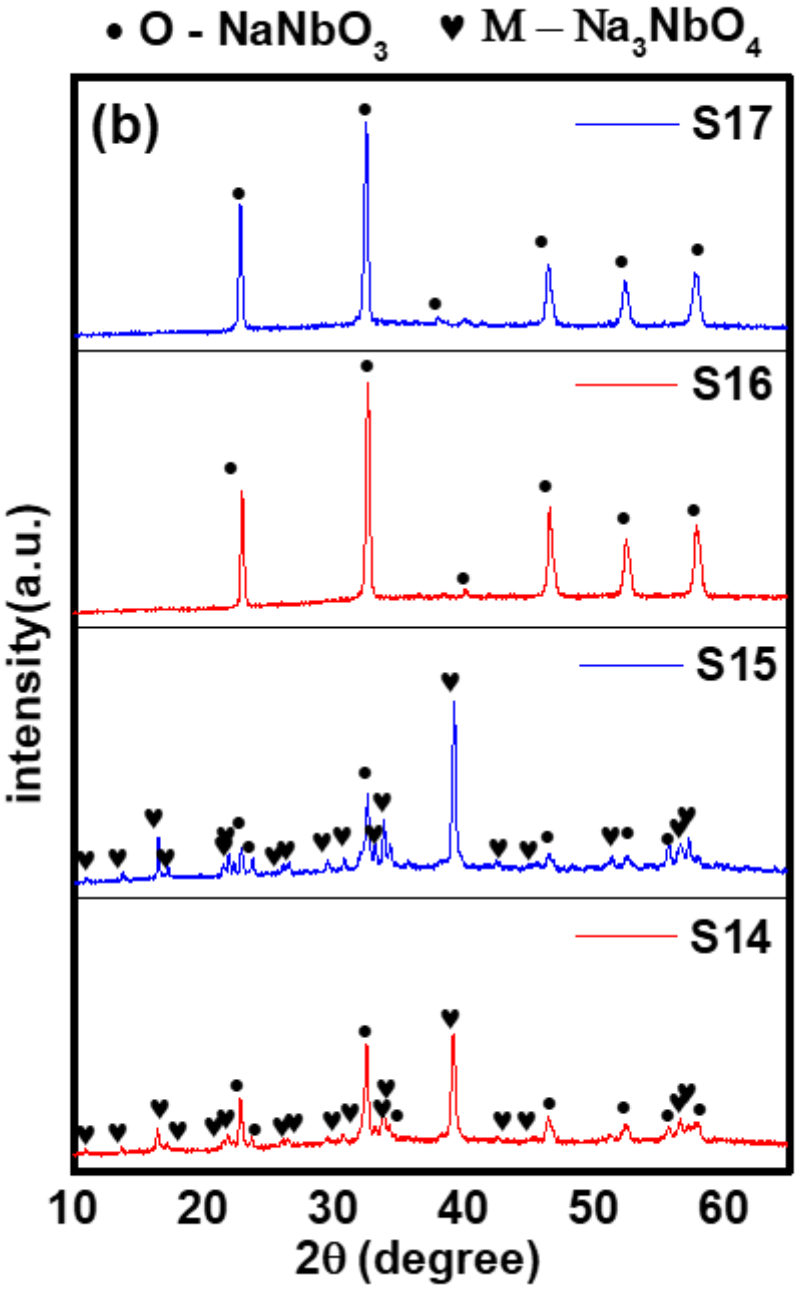

Figure 4.3: Effect of molar ratio on the formation of $NaNbO_3$ at 700 ˚C (red) and 800˚C (blue); (a) 1:10 (S10, S11), 1:15 (S12, S13) and (b) 1:20 (S14, S15), 1:25 (S16, S17).

4.1.2 Preparation of Ca doped $NaNbO_3$: Figure 4.4a represents the XRD patterns of samples with different concentration of dopant i.e. Ca (0.5, 1.0, 1.5, 2.0, 4.0 and 6.0 mol %). All the doped samples consisted of similar diffraction pattern depicting the formation of single phase $NaNbO_3$ with different intensities which may be attributed to the incorporation of Ca in the host lattice.

Enlarged view of (114) peak confirmed the shifting of diffraction peaks towards lower diffraction angle suggesting tensile strain in the host lattice after the attachment of Ca [3]. The most critical observation is the optimization of dopant concentration i.e. 1.0mol% (1.0 Ca) as shown in Figure 4.4b. Upto 1.5mol% (1.5 Ca) doping, there was not much variation in diffraction angle but higher than 1.5mol% resulted to the broadening and high angle shifting of diffraction peaks which can be associated to the detachment of Ca from the host which is not visible in XRD patterns due to small quantity or peak splitting in 6.0 Ca (as shown in **Figure 4.4a**). Moreover, '1.0 Ca' exhibited the most intense diffraction peaks suggesting the optimized concentration of Ca as dopant in $NaNbO_3$ lattice replacing Na atoms. Further, Scherer's and Williamson-Hall method were used to estimate the lattice distortion as an effect of Ca doping [4].

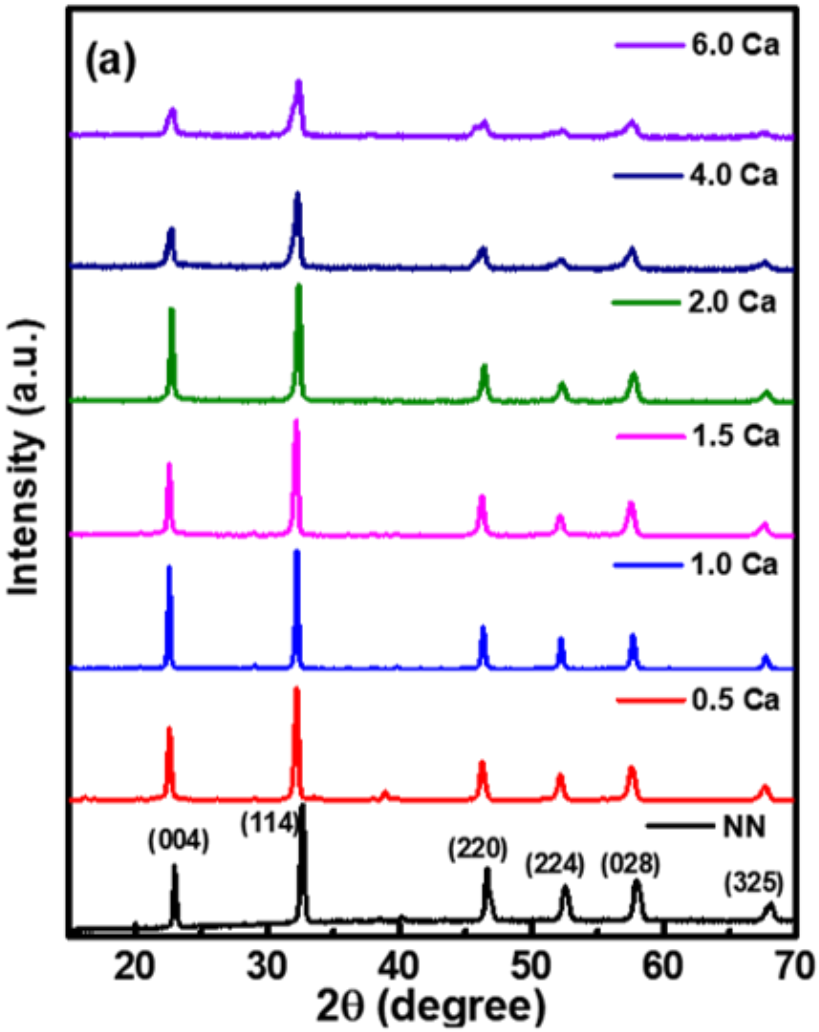

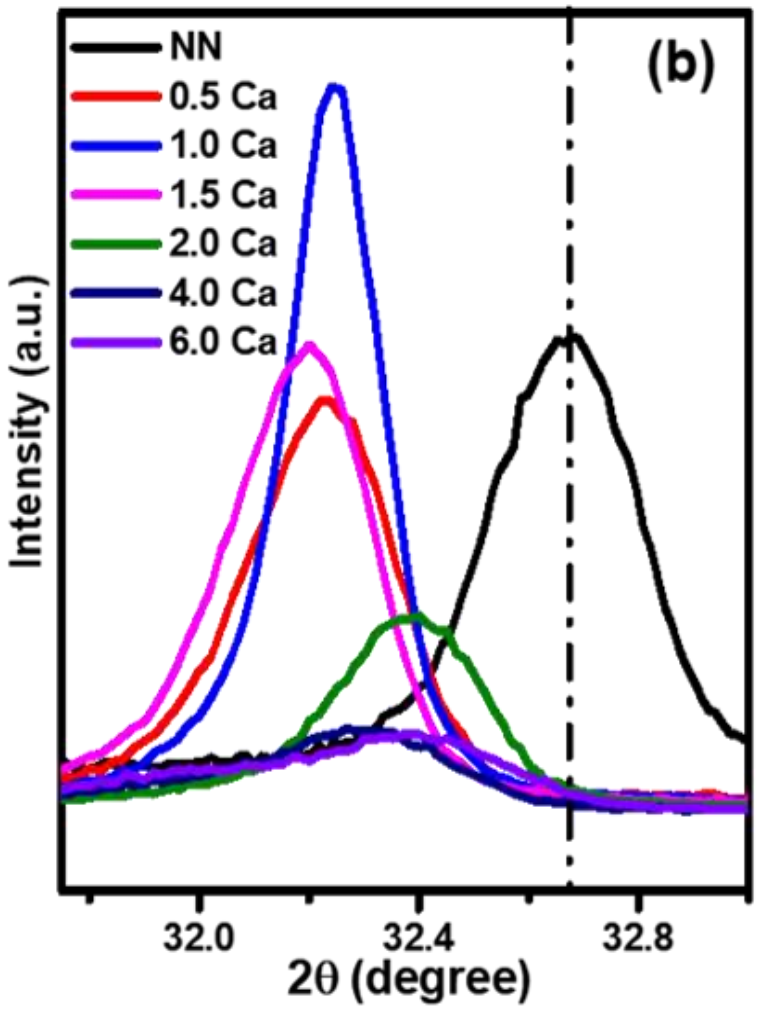

Figure 4.4: (a) XRD pattern of undoped and Ca doped $NaNbO_3$ nanoparticles and (b) magnified XRD pattern to depict the shifting of diffraction peak (114) due to the incorporation of Ca in $NaNbO_3$ lattice.

Table 4.2 represents the crystallite size calculated from Scherer's formula and uniform strain model of W-H analysis. There is not much difference in crystallite sizes but, consideration of lattice distortion makes the applicability of USM more realistic. USM model suggested that doping of Ca led to decrease the lattice strain upto 1.0 Ca containing less distortion as compared to other doped and undoped samples. Moreover, magnitude of lattice strain remains similar in 2.0-6.0mol% samples as suggested by XRD patterns by peak splitting.

Table 4.2: Estimated crystallite size of the synthesized samples using Scherer method

Parameters	**$NaNbO_3$**	**0.5 Ca**	**1.0 Ca**	**1.5 Ca**	**2.0 Ca**	**4.0 Ca**	**6.0 Ca**
Scherer; t (nm)	23.43	22.68	36.68	24.28	22.99	14.40	11.28
USM; t (nm)	19.61	18.79	28.83	20.52	21.63	22.24	23.19
Strain 'ε'× 10^{-3}	3.87	3.20	3.08	4.18	4.44	4.47	4.48

4.2 Electron microscopic analysis (FESEM and TEM)

Figure 4.5 represents the topographical features of undoped (4.5 a, b) and 1.0mol% Ca doped (4.5c, d) $NaNbO_3$ samples. The most interesting feature observed was that the transition of non-faceted to faceted morphology of nanoparticles with Ca doping. Both the micrographs (4.5a, c) suggested the high degree of agglomeration of nanoparticles due to which variation in average particle size has been observed from XRD analysis [5]. TEM study to understand the morphology of nanoparticles which was not clear through FESEM micrographs was done as shown in **Figure 4.6**. It confirmed the presence of agglomerated $NaNbO_3$ nanoparticles in S17 [6].

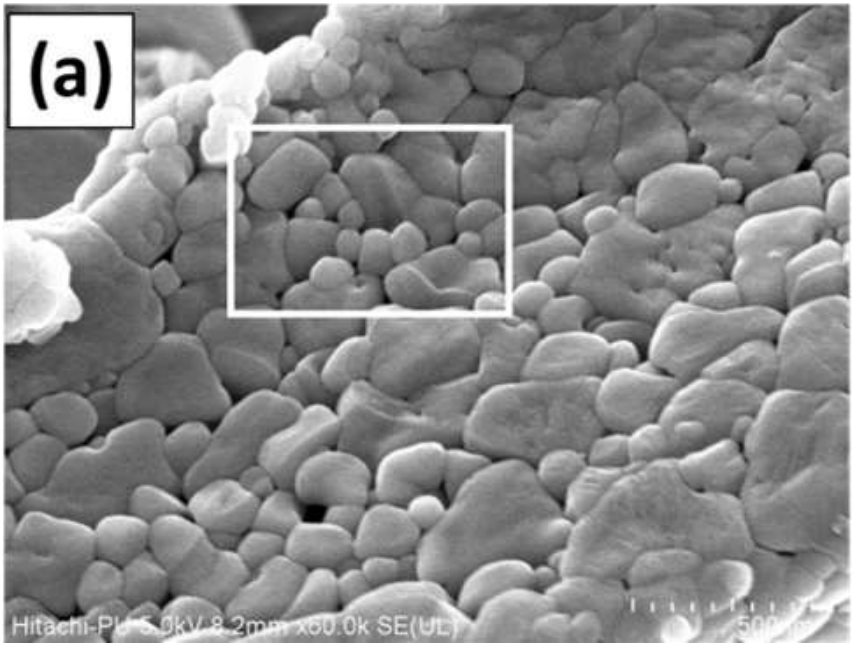

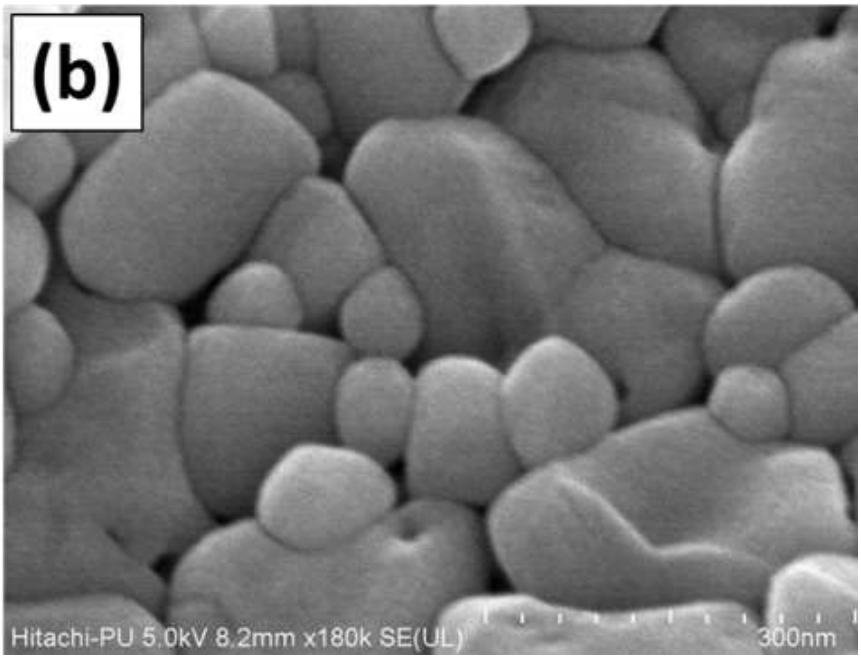
(b)
Hitachi-PU 5.0kV 8.2mm x180k SE(UL)
300nm

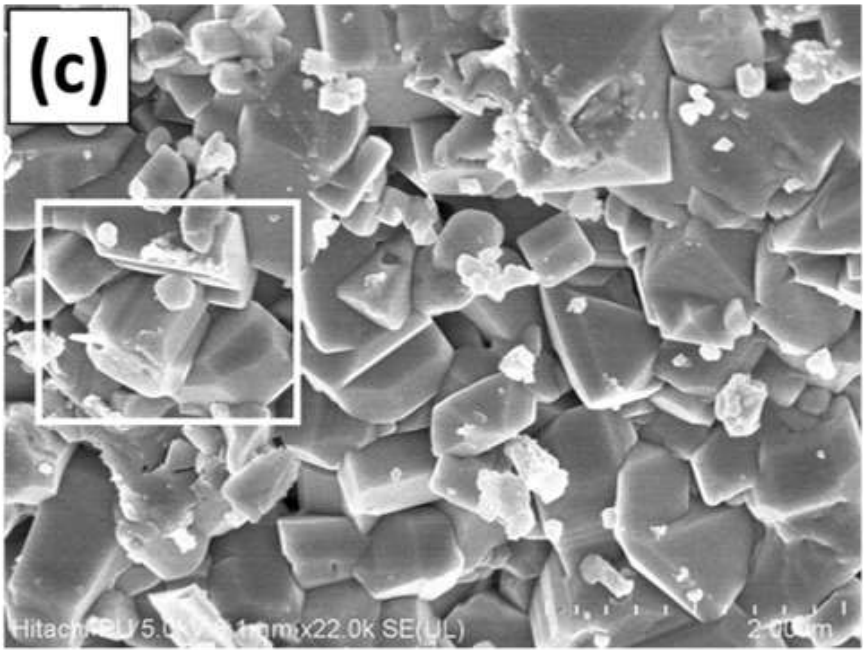
(c)

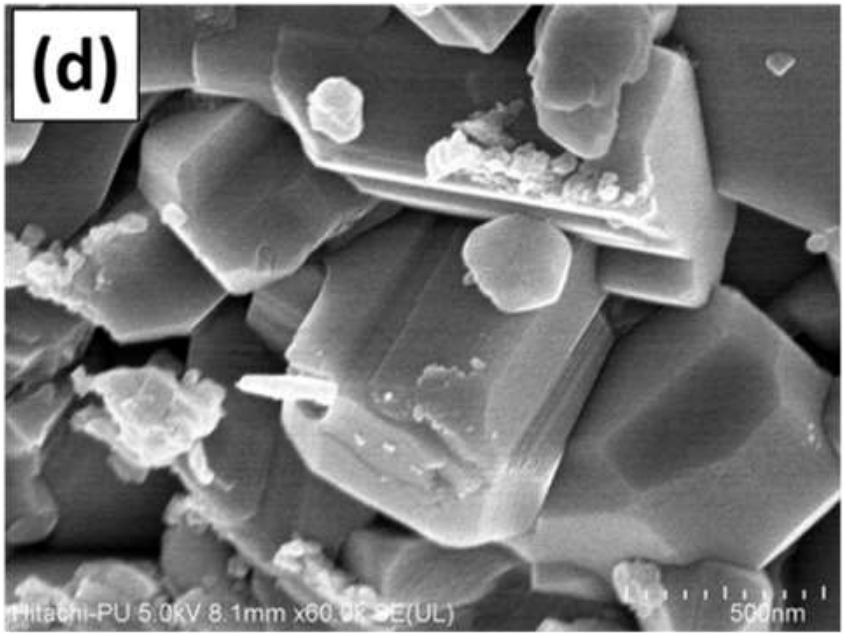

Figure 4.5: FESEM images of (a, b) sample S17 (undoped $NaNbO_3$) and (c, d) 1.0 Ca (1.0mol% Ca doped $NaNbO_3$).

In TEM micrographs particle size and shape exhibits non-faceted morphology as shown in **Figure 4.6 (a, b)**. Moreover, HRTEM micrograph confirmed the formation of $NaNbO_3$ with the help of different lattice fringes as shown in **Figure 4.6 (c, d).** Interplaner spacing d=0.38 and 0.27nm correspond to the plane (004) and (114), respectively suggesting the orthorhombic phase of $NaNbO_3$ [7, 8]. Moreover, average particle size observed from TEM and HRTEM micrographs also supported the calculated values from USM model in the range 15-20nm.

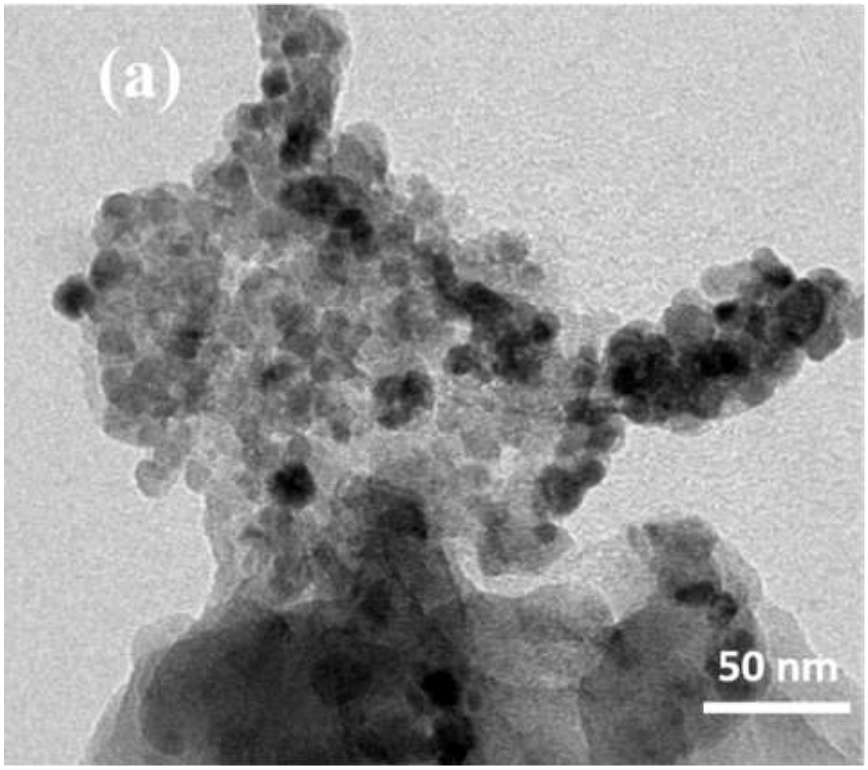
(a)
50 nm

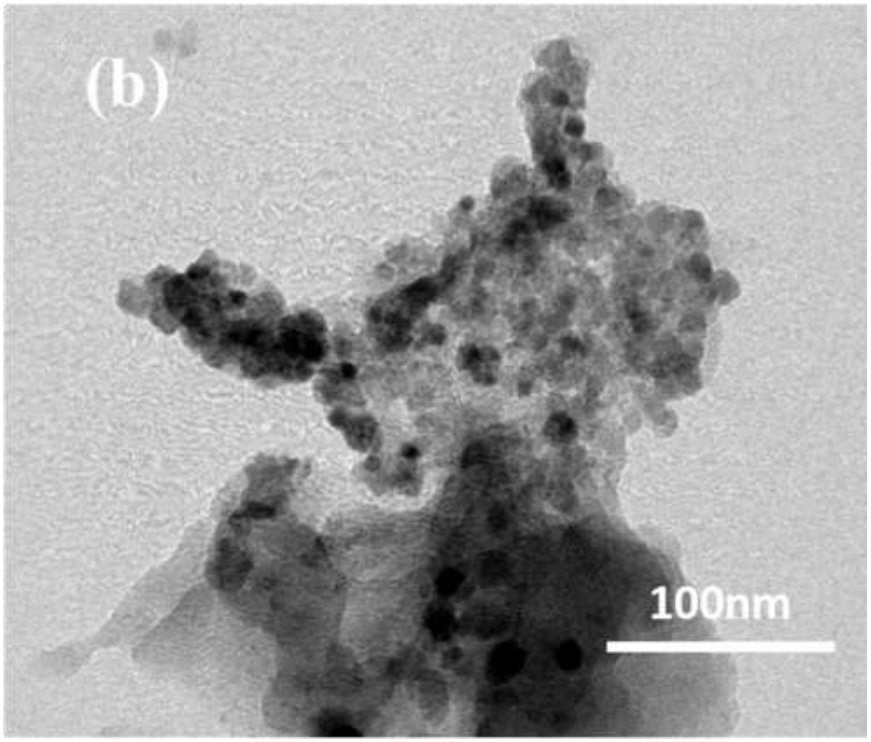
(b)
100nm

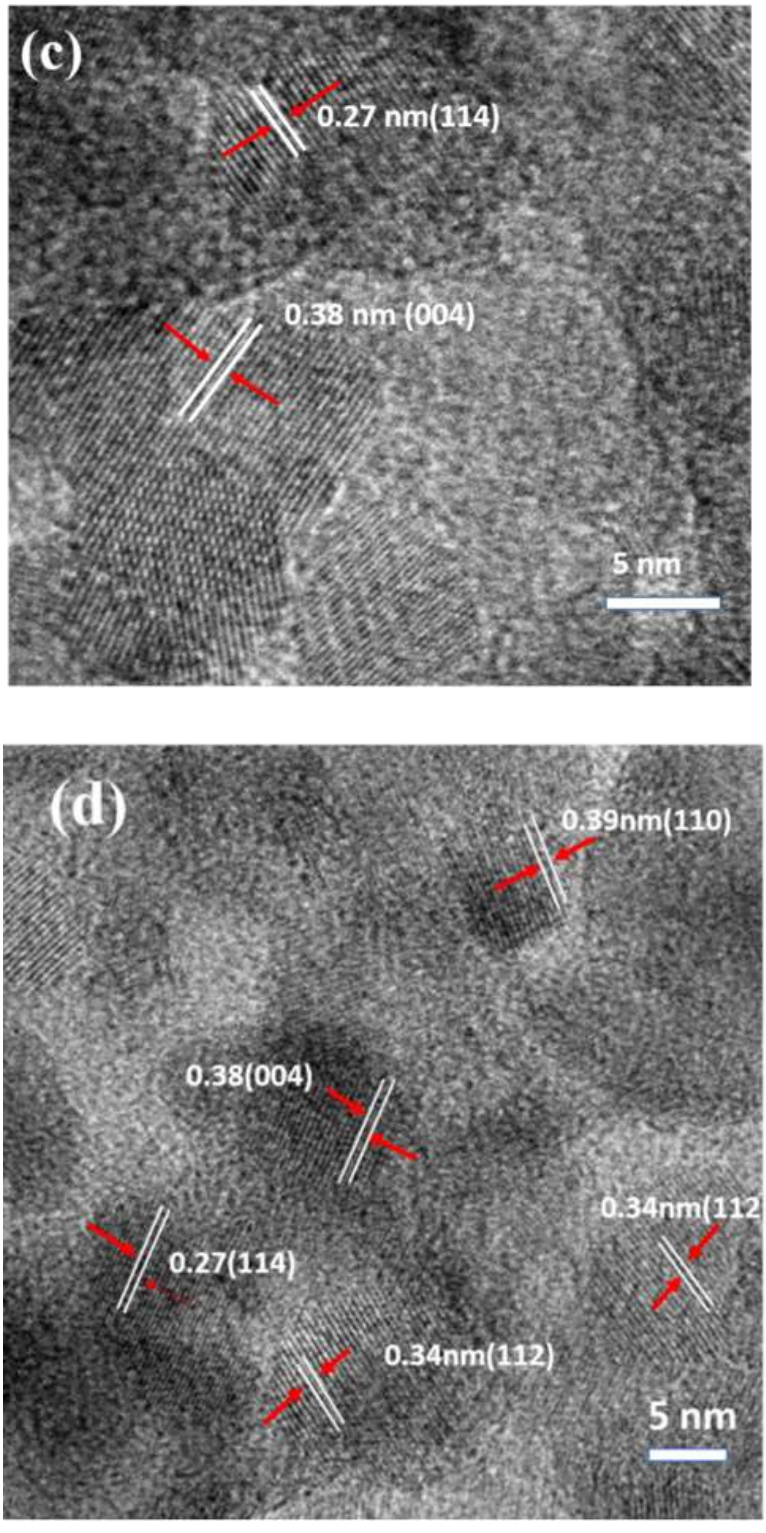

Figure 4.6:(a,b) TEM microstructure of S17 confirming the non-faceted morphology of agglomerated nanoparticles (c, d) HRTEM image of S17 showing the lattice fringes of different planes confirming the formation of $NaNbO_3$.

4.3. Optical analysis

4.3.1 Absorbance spectroscopy:

Figure 4.7a represents the absorbance spectra of undoped and Ca-doped $NaNbO_3$ samples. It has been observed that upto 1.5mol% doping of Ca resulted to the red shift in th absorption edge which got shifted towards lower wavelength beyond 1.5mol% (sample 1.5 Ca). Moreover, the absorption counts also decreased above 1.5mol% as shown in **Figure 4.7a.** With the help of Tauc's plot, optical band gap were also determined which is shown in **Figure 4.7b** and calculate from the intercept (on x-axis) from the tangent on linear portion of graph which has also been listed in **Table 4.3** [9,10]. The observed red shift also resulted to lowering of optical band gap providing the least band gap of 3.37eV for 1.0 Ca sample as compare to other samples.

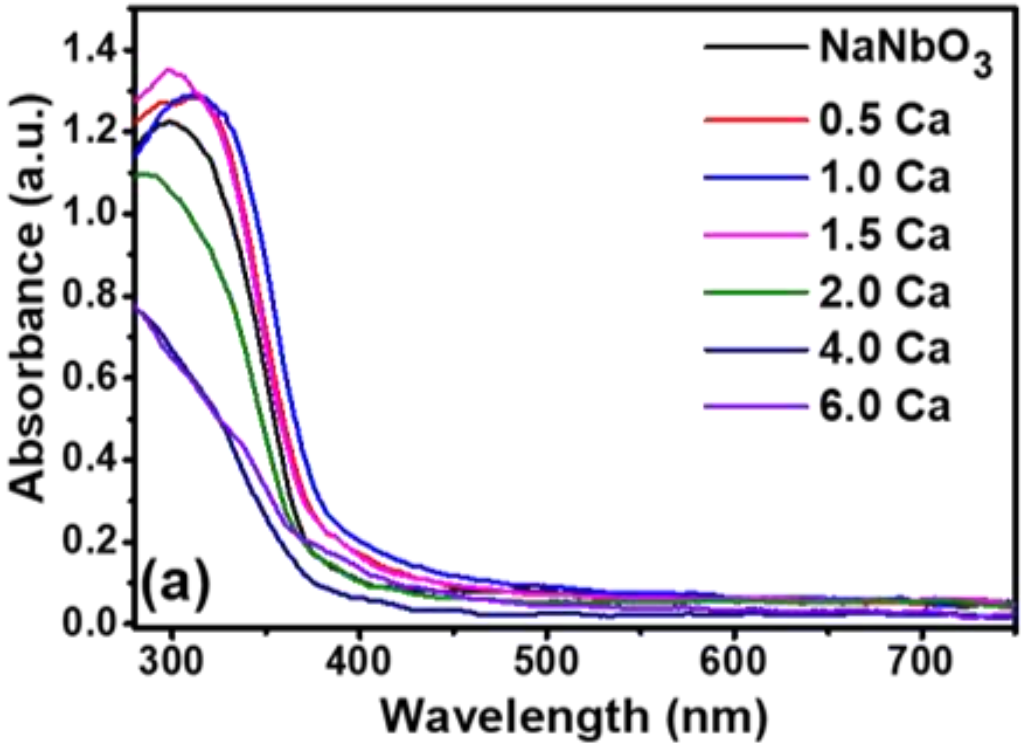

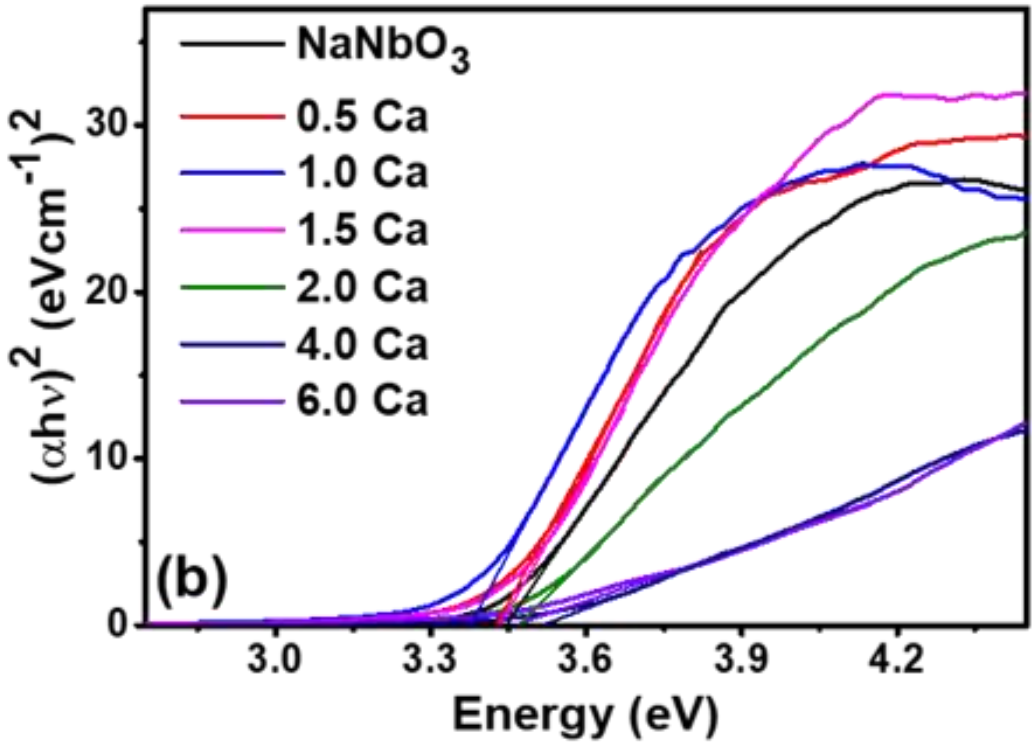

Figure 4.7: (a) UV–visible absorption spectra and **(b)** Tauc's plot for undoped and Ca-doped $NaNbO_3$ samples.

Table 4.3: Band gap energies of Ca doped $NaNbO_3$ nanoparticles

Sample Id	Ca loading concentration (mol %)	Band energy (eV)
S17	0.00	3.44
0.5 Ca	0.50	3.42
1.0 Ca	0.10	3.37
1.5 Ca	0.15	3.43
2.0 Ca	0.20	3.47
4.0 Ca	0.40	3.51
6.0 Ca	0.60	3.46

4.3.2 Photoluminescence spectroscopy:

Figure 4.8 represents the emission spectra of undoped $NaNbO_3$ (S17) under the UV-excitation of 280nm in the range of 300-500nm [11]. The emission bands are observed centered at 360, 380 and 405nm. The peak intensity at 380nm was prominent as compared to the other peaks. The PL peaks attributed due to one transition between O^{2-} and Nb^{5+}. It is based on the local structure of NbO_6 octahedra. The NbO_6 octahedra possess high degree of symmetry lacking oxygen vacancies or

distortions which are changing the clusters of organizations. In addition to this, order-disorder transitions, $NaNbO_3$ offers symmetry rupture along the O-Nb-O, resulting into complex clusters with $[NbO_6]$-$[NbO_5]$ distribution in the $[NbO_6]$-$[NbO_6]$ octahedra. The visible band at 405 in the emission spectra is characterized property of ABO_3 pervoksites [12, 13].

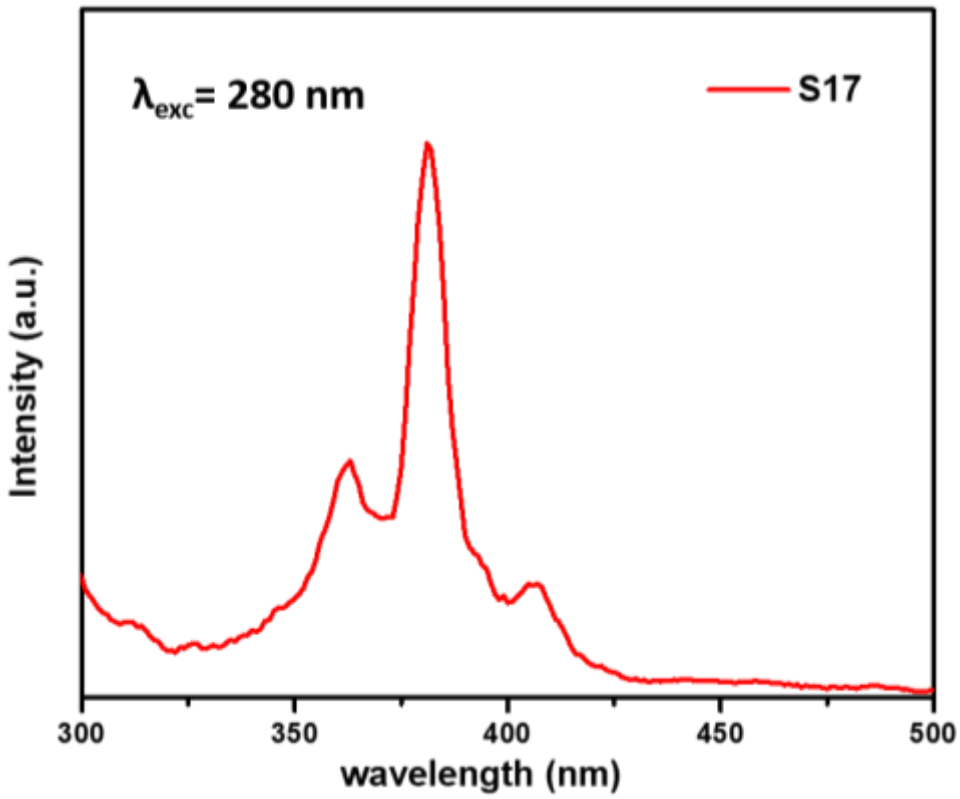

Figure 4.8: Photoluminescence spectra of sample S17.

4.4 Photocatalytic activity

Figure 4.9 represents the decreasing absorbance spectra of MB dye with respect to irradiation time. In all the spectra, black calibration curve depicts the absorption of 1mg/L concentration of MB dye. Thereafter, the establishment of adsorption-desorption equilibrium under dark chamber was carried out with three different concentration of photocatalyst (200, 400 and 600mg/L) as shown in **Figure 4.9(a-c)** (respectively with red line). Such decrement in the concentration of MB dye in supernatant can be associated to the absorption of dye molecules on the surface of photocatalyst which came to be 12.3%, 13.3% and 12.5% for 200mg/L, 400mg/L and 600mg/L respectively. It has been observed that there was slight variation in the absorption capacity of as-synthesized photocatalyst [14].

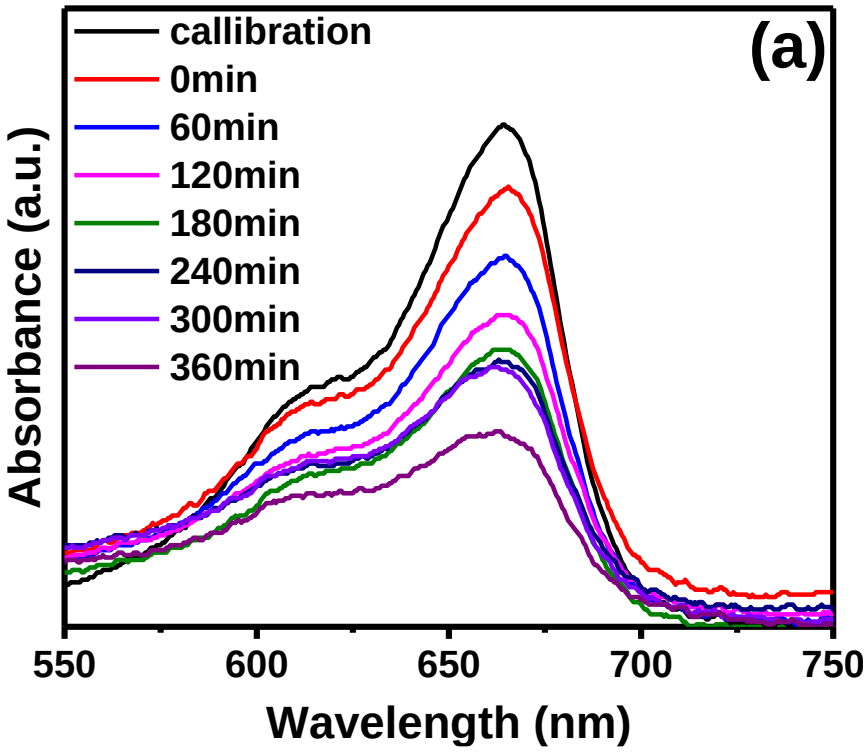
(a)
callibration
0min
60min
120min
180min
240min
300min
360min
Absorbance (a.u.)
550
600
650
700
750
Wavelength (nm)

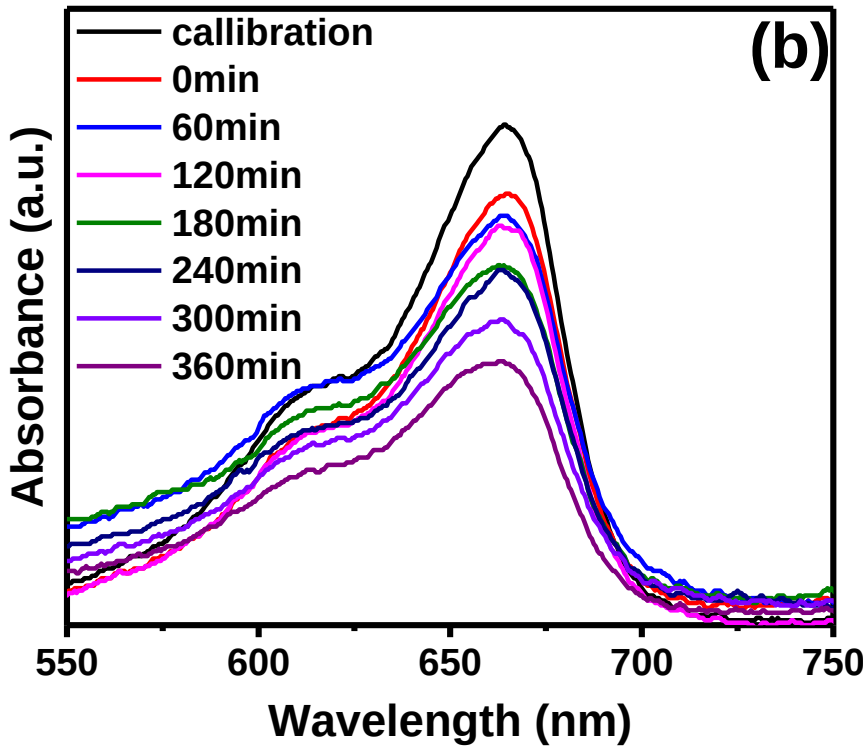
(b)
callibration
0min
60min
120min
180min
240min
300min
360min
Absorbance (a.u.)
550
600
650
700
750
Wavelength (nm)

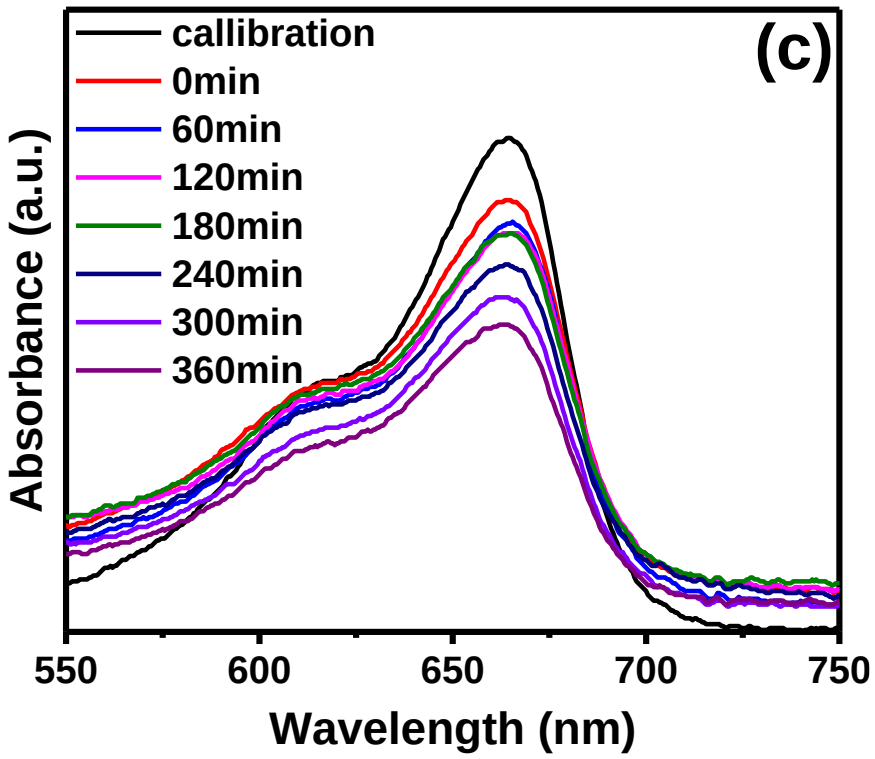

Figure 4.9: Absorption spectra of MB dye aqueous solution (1mg/L) degraded by different concentration of S17; (a) 200mg/L, (b) 400mg/L and (c) 600mg/L.

Further, illumination of visible light for 6h resulted to the decrement to the concentration of MB dye in the solution which might be associated to the absorption or photo degradation of MB dye. The respective decrement in concentration of MB dye is shown in **Figure 4.10 (a)** as C/C_0 vs. irradiation time where C_0 and C represent the concentration of MB dye at time = 0 and 't' min, respectively. Further, percent degradation has also been calculated and is shown in **Figure 4.10 (b)** in which it can be clearly seen observed that 400mg/L concentration of photocatalyst (S17) has performed better than other two concentrations showing ~47% efficiency [15]. The decreased efficiency (28.6%) of higher concentration (600mg/L) of S17 might be attributed to the slightly decreased adsorption and enhanced hindrance to the penetration of light into the solution to excite the photocatalyst generating the electron-hole pair. Therefore, 400mg/L of S17 has been considered as optimized concentration of photocatalyst for further studies under similar conditions.

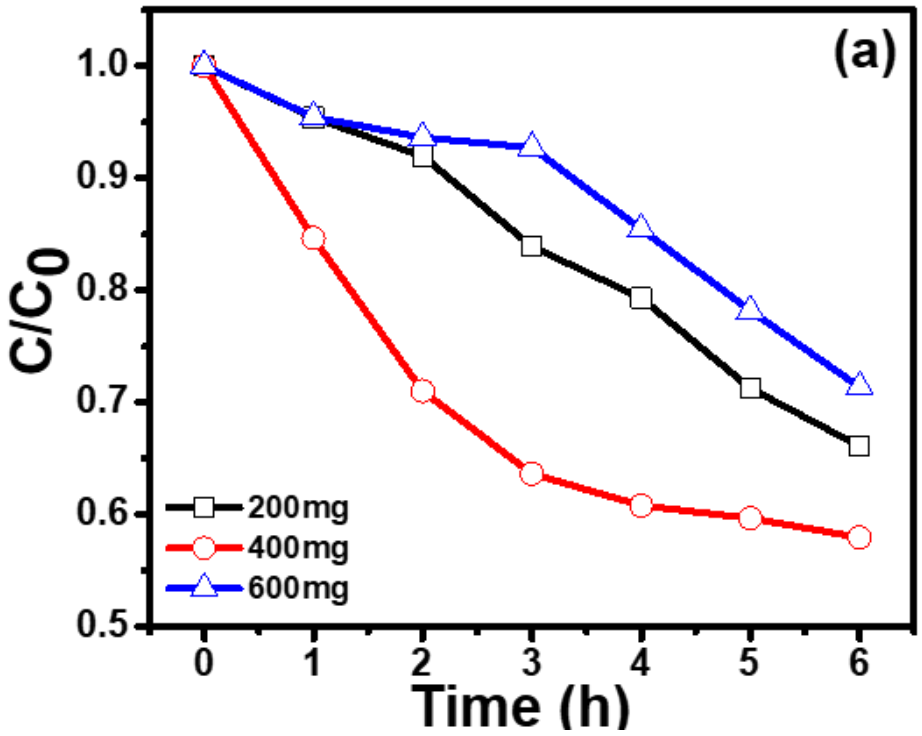
(a)
C/C0
1.0
0.9
0.8
0.7
0.6
0.5
200mg
400mg
600mg
0
1
2
3
4
5
6
Time (h)

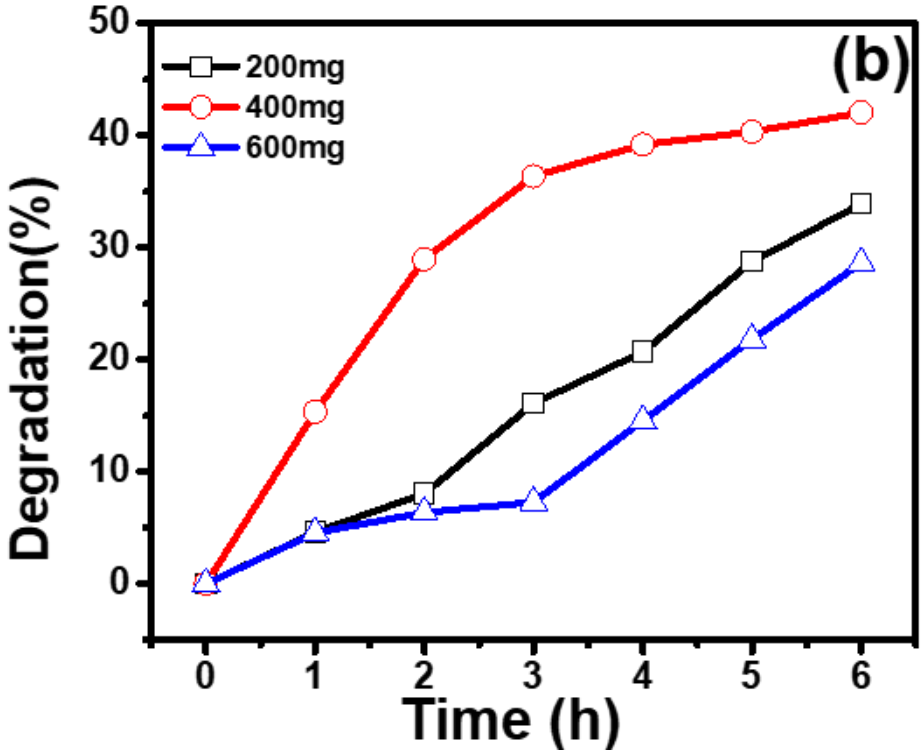
(b)
Degradation(%)
50
40
30
20
10
0
200mg
400mg
600mg
0
1
2
3
4
5
6
Time (h)

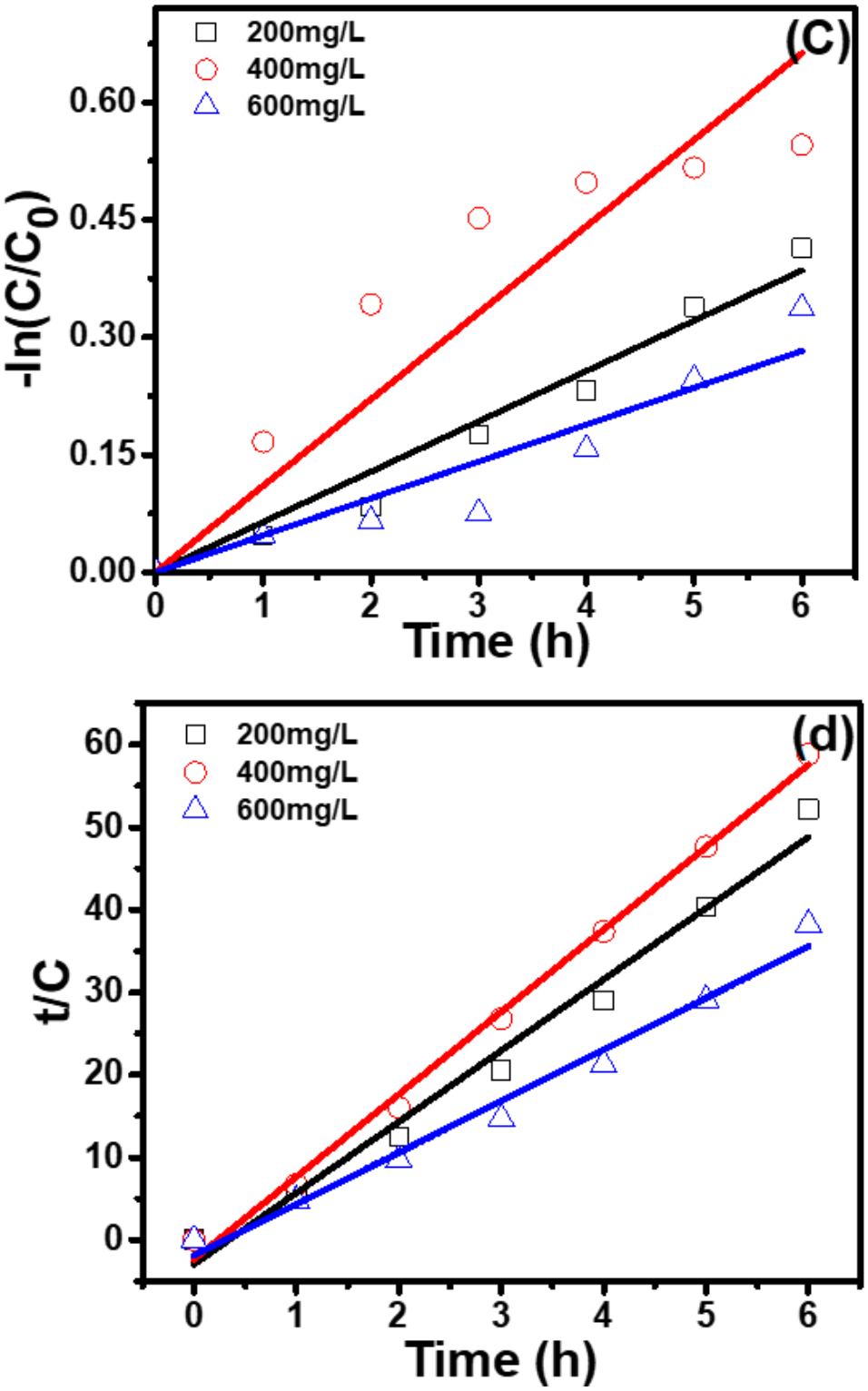

Figure 4.10: (a) Relative change in MB concentration, (b) percent degradation, (c) pseudo first order and (d) second order kinetics of MB degradation in the presence of different concentration of S17.

The photocatalytic decomposition of MB dye on the surface of $NaNbO_3$ nanoparticles has been analyzed with the help of photo reaction kinetics (pseudo first and second order). Pseudo first order and second order kinetics assume the absorption of dissolved molecule on the surface of substrate via physisorption and chemisorption, respectively which can also be explained by following mathematical equations:

Pseudo first order $$-ln(C/C_0) = K_1 t \quad (1)$$

Pseudo second order $$t/C = \left(1/K_2 C_0^2\right) + t/C_0 \quad (2)$$

Where C, C_0, t has their usual meanings and K_1, K_2 represent the rate constants in pseudo first and second order kinetic law, respectively. Moreover, the magnitude of K_1 and K_2 can be determined by plotting -ln C/C_0 vs. t and t/C vs. t (respectively) as shown in **Figure 4.10 (c, d)** and **Table 4.4**. With the increase in the concentration of S17 from 200mg/L to 400mg/L, photochemical reaction rate has been increased, but it got decreased on further increment in concentration i.e. 600mg/L. Further, quality of fitting (R^2) suggested the simultaneous processes of sorption (physi- and chemisorption) as R^2>0.9 in all the cases.

Further, to study the effect of Ca doping in $NaNbO_3$ on the photocatalytic performance of the host, 400mg/L was kept as concentration of doped Photocatalysts under similar conditions. **Figure 4.11(a, b)** represent the relative change and degradation (%) of the MB dye, respectively. **Figure 4.11(b)** suggested the higher degradation efficiency (~54%) of 1.0 Ca than bare host i.e. $NaNbO_3$ (S17) which can be co-related to the incorporation of Ca^{2+} ions in host lattice inducing some oxygen vacancies or entrapment of charge carriers [16]. While, rest of the other doped sample performed lesser than bare host sample. Further, reaction kinetic studies revealed the similar nature of simultaneous physi- and chemisorption during the photo degradation of MB dye with K_1=0.1285h^{-1} and K_2=5.3806h^{-1}, respectively, as shown in **Figure 4.11(c, d).**

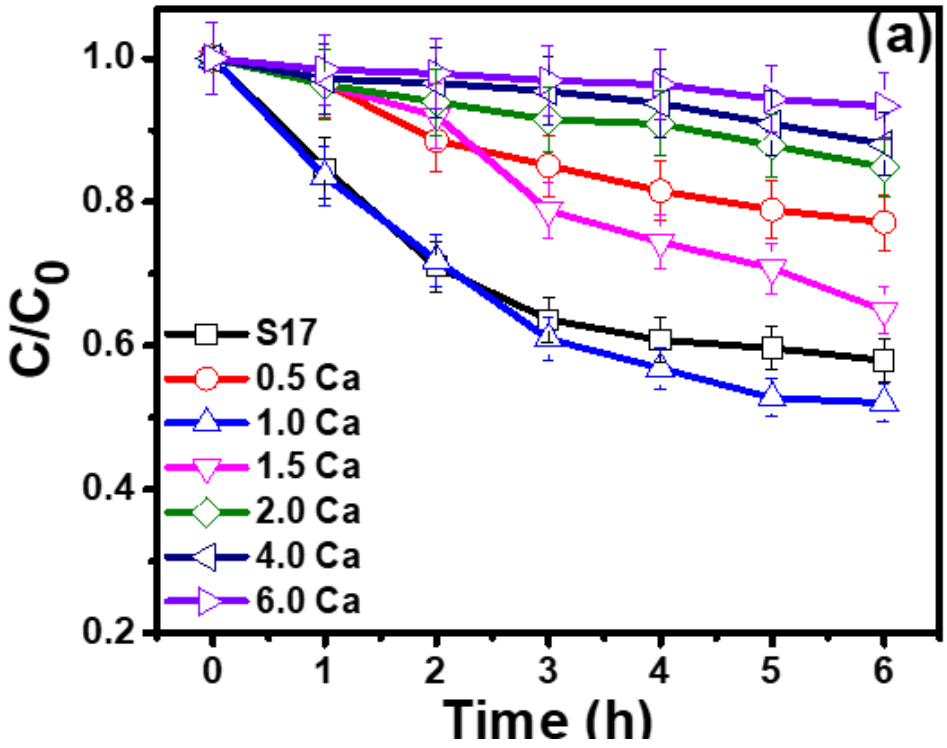
(a)
C/C0
Time (h)
S17
0.5 Ca
1.0 Ca
1.5 Ca
2.0 Ca
4.0 Ca
6.0 Ca

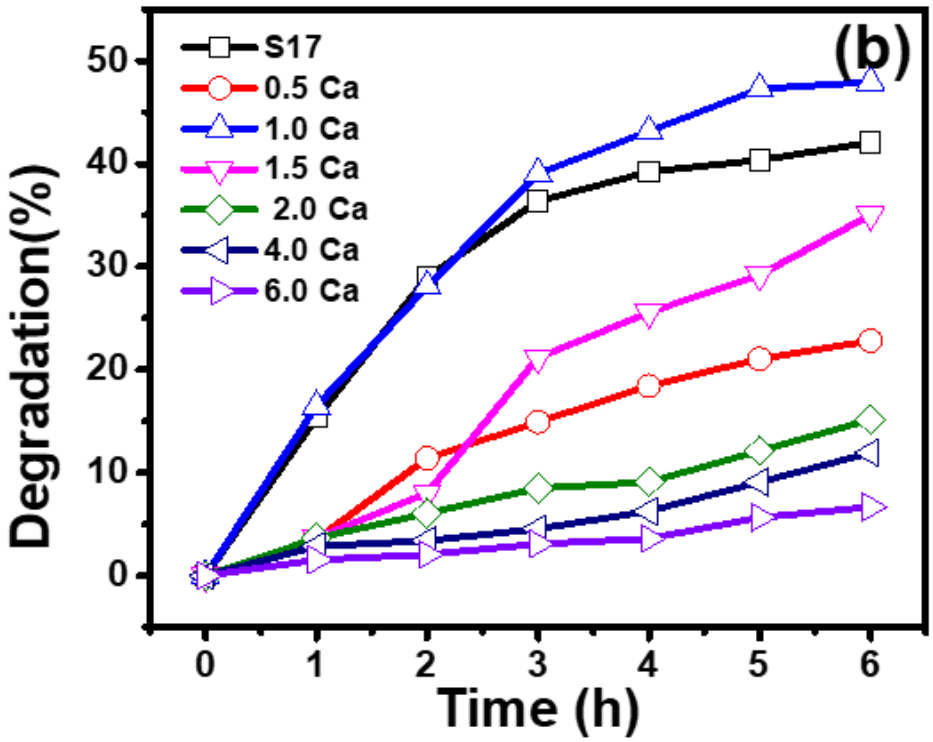
(b)
Degradation(%)
Time (h)
S17
0.5 Ca
1.0 Ca
1.5 Ca
2.0 Ca
4.0 Ca
6.0 Ca

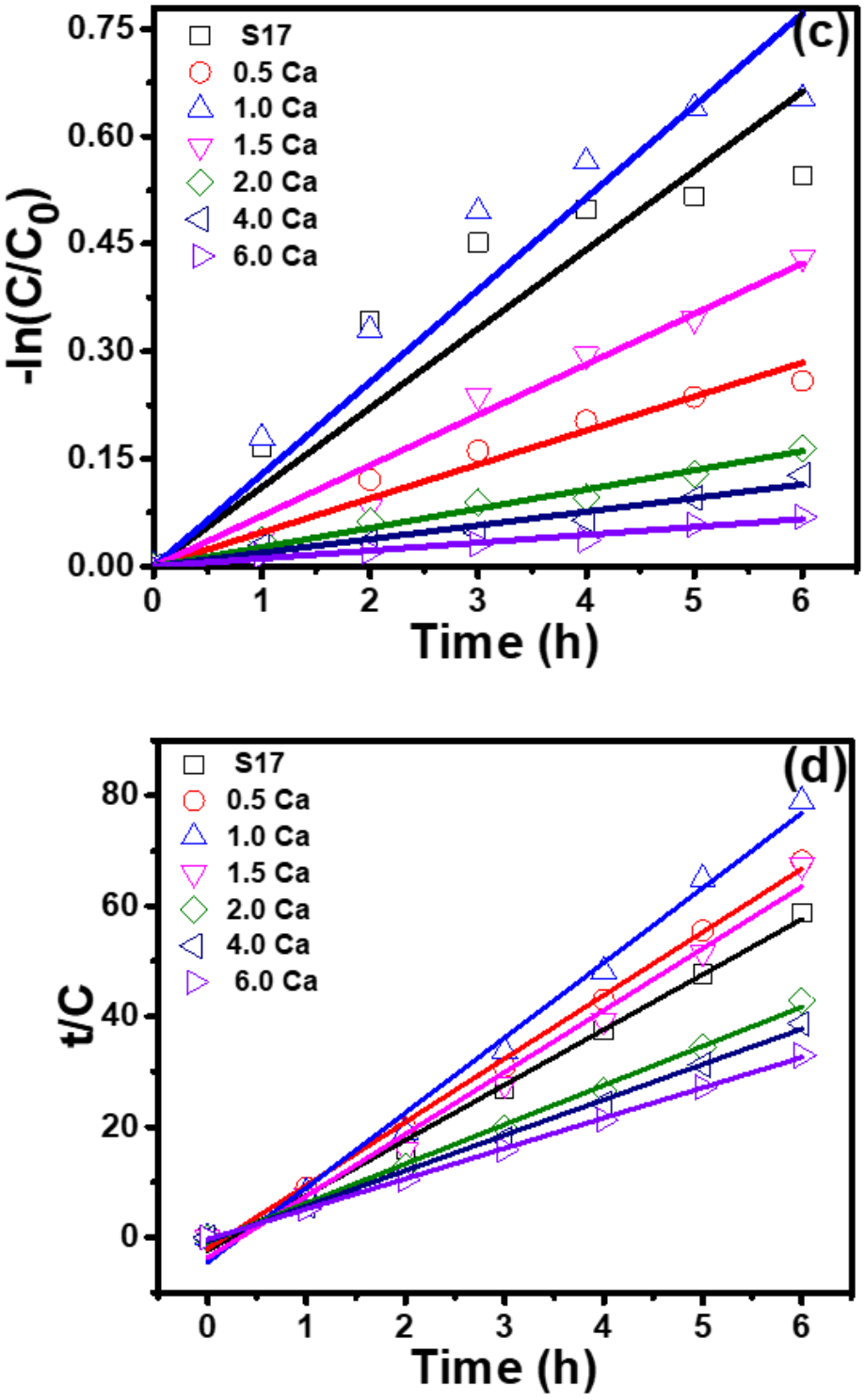

Figure 4.11: (a) Relative change in MB concentration, (b) percent degradation, (c) pseudo first order and (d) second order kinetics of MB degradation in the presence of Ca doped S17 samples.

Table 4.4: Reaction rate constants of photo degradation of MB dye.

S. No.	Catalyst	Concentration (mg/L)	Pseudo-first order		Pseudo-second order	
			K_1 (h^{-1})	R_1^2	K_2 (h^{-1})	R_2^2
1.	S17	200	0.0668	0.96	8.2287	0.98
2.	S17	400	0.1279	0.98	10.3437	0.99
3.	S17	600	0.0471	0.95	8.1067	0.98
4.	Ca 0.5	400	0.0473	0.98	12.1881	0.99
5.	Ca 1.0	400	0.1285	0.97	5.3806	0.99
6.	Ca 1.5	400	0.0704	0.98	6.5995	0.98
7.	Ca 2.0	400	0.0268	0.99	28.4484	0.99
8.	Ca 4.0	400	0.0190	0.98	34.7658	0.99
9.	Ca 6.0	400	0.0110	0.98	75.3619	0.99

References

1. A.Gupta, O.P. Pandey, Visible irradiation induced photo degradation by NbC/C Nano composite derived from smoked cigarette litter (filters), Solar Energy 163 (2018) 167–176.

2. S. Chakraborty, B. K. Sarkar , S. K. Ghosh , G. C. Das, S. Mukherjee, Phase evolution, morphology and photo degradation kinetics of hydrothermally synthesized tetragonal sodium niobate, J Aust Ceram Soc 53 (2013) 687-699.

3. M. Mittal, M. Sharma, O.P. Pandey, Fast and quick degradation properties of doped and capped ZnO nanoparticles under UV–Visible light radiations, Solar Energy 125 (2016) 51-56.

4. N. Chaiyo, R. Muanghlua, S. Niemcharoen, B. Boonchom, N. Vittayakorn ,Solution combustion synthesis and characterization of lead-free piezoelectric sodium niobate ($NaNbO_3$) powder, Journal of alloys and compounds 509 (2011) 2445-2449.

5. N. Chaiyo, B. Boonchom, N. Vittayakorn, Solid-state reaction synthesis of sodium niobate ($NaNbO_3$) powder at low temperature, J Mater Sci 45 (2010) 1443–1447.

6. A.S Attar , E.S Sichani, S. Sharafi, Structural and dielectric properties of Bi-doped barium strontium titanate nanopowder synthesized by sol–gel method, Journal of material science and technology 6 (2017) 1-8.

7. C. Shifu, J. Lei, T. Wenming , F .Xianliang , Fabrication, characterization and mechanism of a novel Z-scheme photocatalyst $NaNbO_3/WO_3$ with enhanced photocatalytic activity, The Royal Society of Chemistry 42 (2013) 10759–10768.

8. H. Shi, X. Li, D. Wang, Y. Yuan, Z. Zou, J. Ye, $NaNbO_3$ Nanostructures: Facile Synthesis, Characterization, and Their Photocatalytic Properties, Catal Lett 132 (2009) 205–212.

9. J. Kaur, M. Sharma, O.P.Pandey, Structural and optical studies of undoped and copper doped zinc oxide nanoparticles for photocatalytic applications, Superlattices and microstructure 77 (2015) 35-53.

10. P. Li, H. Abe, J. Ye, Band-Gap Engineering of $NaNbO_3$ for Photocatalytic H_2 Evolution with Visible Light, International Journal of Photo energy vol. 2014 (2014) 1-7.

11. E.S.Baeissa, Photocatalytic degradation of malachite green dye using Au/NaNbO3 nanoparticles, Journal of alloys and components 672 (2016) 564-570.

12. S.chen, Y.Hu ,L.Ji, X.Jihang.X.hu, Preperation and characterization of direct Z-scheme photocatalyst $Bi_2O_3/NaNbO_3$ and its reaction mechanism, Applied surface science 292 (2014) 357-366.

13. G. F. Teixeiran, T. R. Wright, D. C. Manfroi, E. Longo, J. A. Varela, M. A. Zaghete, Photoluminescence in NaNbO3 particles and films, Materials letters 139 (2015) 443-446.

14. M. Mittal , M. Sharma , O.P. Pandey , UV–Visible light induced photocatalytic studies of Cu doped ZnO nanoparticles prepared by co-precipitation method, Solar Energy, 110 (2014) 386–397.

15. M. Mittal, M. Sharma, O.P.Pandey, Photocatalytic Studies of crystal violet dye using Mn doped and PVP capped ZnO Nanoparticles, Journal of Nano science and Nanotechnology 14 (2014) 2725-2733.

16. M. Mittal, A. Gupta, O.P. Pandey, Role of oxygen vacancies in Ag/Au doped CeO_2 nanoparticles for fast photocatalysis, Solar Energy 165 (2018) 206–216.

5. Conclusion

In this work, we have synthesized $NaNbO_3$ nanoparticle successfully via chemical precipitation route, using sodium sulphide as a sodium source and ammonium niobate oxalate hydrate as niobium source. The nanostructured $NaNbO_3$ particles were characterized XRD, FESEM, TEM, UV-visible, PL and photocatalytic activity. Among all the samples, the sample (S17) synthesized at 800˚ C for 5h, with the different amount of molar ratios of Nb: Na (1:/1,2,6,10,15,20, 25) (sample S17) was pure single phase $NaNbO_3$, revealed by XRD patterns matched with the standard ICDD card (01-073-0803). The crystallite size was calculated by the Scherer method with average crystallite size 23.4 nm. FESEM microstructure revealed irregular microstructure and with two type of size distribution in the range of 60-80nm and 100-200nm. HRTEM micrographs depicted agglomeration in the particle and d-spacing value of lattice fringes was 0.38 nm corresponding to the (004) which confirmed the formation of $NaNbO_3$ nanoparticles. The optical studies of the synthesized sample S17 showed a band gap of 3.44 eV, calculated with the help of Kubelka munk method. The prominent PL peak observed at 380nm wavelength which is in the visible region along with the small peaks at 360 nm and 405 nm undergoes excitation at 280nm. The prepared $NaNbO_3$ nanoparticles were also tested as photo catalyst degradation of organic pollutants i.e. methylene blue dye (MB). The photocatalytic activity of sample S17 has been successfully studied for $NaNbO_3$ nanoparticles synthesized at different amount of $NaNbO_3$ powder (200mg/L, 400mg/L and 600mg/L), it has been found that $NaNbO_3$ nanoparticles synthesized at 200mg/L and 600mg/L of $NaNbO_3$ degrades of 37.9% and 28.6% of MB dye after 5h under visible light but 400mg of $NaNbO_3$ degrades 51.7% dye so it shows better degradation. Ca doped samples with the different concentration (0.5-2%, 4%, 6%) in 400mg/L were prepared. It has been found that Ca (1%) doped nanoparticles shows the degradation of 54% of dye under the exposer of visible light. However, undoped and other Ca doped nanoparticles shows lesser degradation than Ca(1%) doped nanoparticle. Loading of catalyst shows that 1.0g/L of catalyst shows maximum photo degradation of MB dye.

6. Future scope

$NaNbO_3$ nanoparticles can also be synthesized by using different sodium sources in which synthesized parameter like temperature, time and molar ratio can be optimized. In our study, we have doped Ca in $NaNbO_3$ nanoparticles, similarly doping of other divalent ions can also be studied. $NaNbO_3$ nanoparticles can also be synthesized at different pH values to study their effect on photocatalytic as well as optical properties